Branch Cuts of Stokes Wave on Deep Water. Part I: Numerical Solution and Padé Approximation

By S. A. Dyachenko, P. M. Lushnikov, and A. O. Korotkevich

Complex analytical structure of Stokes wave for two-dimensional potential flow of the ideal incompressible fluid with free surface and infinite depth is analyzed. Stokes wave is the fully nonlinear periodic gravity wave prop agating with the constant velocity. Simulations with the quadruple (32 digits) and variable precisions (more than 200 digits) are performed to find Stokes wave with high accuracy and study the Stokes wave approaching its limiting form with $2\pi/3$ radians angle on the crest. A conformal map is used that maps a free fluid surface of Stokes wave into the real line with fluid domain mapped into the lower complex half-plane. The Stokes wave is fully characterized by the complex singularities in the upper complex half-plane. These singularities are addressed by rational (Padé) interpolation of Stokes wave in the complex plane. Convergence of Padé approximation to the density of complex poles with the increase in the numerical precision and subsequent increase in the number of approximating poles reveals that the only singularities of Stokes wave are branch points connected by branch cuts. The converging densities are the jumps across the branch cuts. There is one square-root branch point per horizontal spatial period λ of Stokes wave located at the distance v_c from the real line. The increase in the scaled wave height H/λ from the linear limit $H/\lambda = 0$ to the critical value H_{max}/λ marks the transition from the limit of almost linear wave to a strongly nonlinear limiting Stokes wave (also called the Stokes wave of the greatest height). Here, H is the wave height from the crest to the trough in physical variables. The limiting Stokes wave emerges as the singularity reaches the

Address for correspondence: Pavel M. Lushnikov, Department of Mathematics and Statistics MSC01 1115, 1 University of New Mexico, Albuquerque, New Mexico, 87131-0001, USA; e-mail: plushnik@math.unm.edu

DOI: 10.1111/sapm.12128

STUDIES IN APPLIED MATHEMATICS 137:419–472

fluid surface. Tables of Padé approximation for Stokes waves of different heights are provided. These tables allow to recover the Stokes wave with the relative accuracy of at least 10^{-26}. The number of poles in tables increases from a few for near-linear Stokes wave up to about hundred poles to highly nonlinear Stokes wave with $v_c/\lambda \sim 10^{-7}$.

1. Introduction

Theory of spatially periodic progressive (propagating with constant velocity without change of the shape and amplitude) waves in two-dimensional (2D) potential flow of an ideal incompressible fluid with free surface in gravitational field was founded in pioneering works by Stokes [1, 2] and developed further by Michell [3], Nekrasov [4,5], and many others (see, e.g., a book by Sretenskii [6] for review of older works as well as works [7–16] and references therein for more recent progress).

Stokes wave is important in oceanology because a slow approaching of Stokes wave over time to its limiting form during wave dynamics is one of the possible routes to wave breaking and whitecapping, which are responsible for significant part of energy dissipation for gravity waves [17, 18]. Here, by slow approaching, we mean the time scale which is much larger than the temporal period of the gravity wave of the same spatial period as for the given Stokes wave. Formation of a close to limiting Stokes wave is also considered to be a probable final stage of evolution of a freak (or rogue) waves in the ocean resulting in the formation of approximate limiting Stokes wave for a limited period of time with following wave breaking and disintegration of the wave or whitecapping and attenuation of the freak wave into wave of regular amplitude [19,20].

There are two major approaches to analyze the Stokes wave, both originally developed by Stokes. The first approach is the perturbation expansion in amplitude of Stokes wave called by the Stokes expansion. That approach is very effective for small amplitudes but converges very slowly (or does not converge at all, depending on the formulation according to [21]) as the wave approaches the maximum height $H = H_{max}$ (also called by the Stokes wave of the greatest height or the limiting Stokes wave). Here, the height H is defined as the vertical distance from the crest to the trough of Stokes wave over a spatial period λ. The second approach is to consider the limiting Stokes wave, which is the progressive wave with the highest nonlinearity. Using conformal mappings, Stokes found that the limiting Stokes wave has the sharp angle of $2\pi/3$ radians on the crest [22], i.e., the surface is nonsmooth (has a jump of slope) at that spatial point. That corner singularity explains a slow convergence of Stokes expansion as

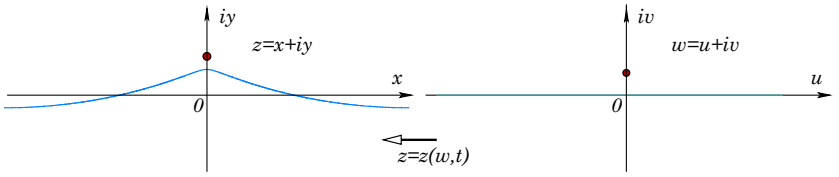

Figure 1. Schematic of a conformal map between the domain below the solid curve (left panel) in $z = x + \mathrm{i}y$ complex plane and the lower complex half-plane in $w = u + \mathrm{i}v$ (right panel). Fluid occupies the domain below the solid curve in physical plane $z = x + \mathrm{i}y$. The solid curve of left panel (corresponds to a free surface of the fluid) is mapped into the real line (another solid line) in right panel. One spatial period of Stokes wave is shown by solid lines in both panels in the reference frame moving with the velocity c. The dark circles mark the positions of the singularity closest to the fluid surface in both panels.

$H \to H_{max}$. The global existence of the limiting Stokes wave was proven in [23], however, lacking a proof of a Stokes conjecture that the jump of the slope at the crest is exactly $2\pi/3$ radians. The Stokes conjecture was later independently proven in Refs. [24] and [25].

It was Stokes [22] who first proposed to use conformal mapping to address finite amplitude progressive waves. In this paper, we consider a particular case of potential flow of the ideal fluid of infinite depth although more general case of fluid of arbitrary depth can be studied in a similar way. Assume that free surface is located at $y = \eta(x, t)$, where x is the horizontal coordinate, y is the vertical coordinate, t is the time, and $\eta(x, t)$ is the surface elevation with respect to the zero mean level of fluid, i.e., $\int_{-\infty}^{\infty} \eta(x, t)\mathrm{d}x = 0$. We consider the conformal map between the domain $-\infty < y \le \eta(x, t),\ -\infty < x < \infty$ of the complex plane $z \equiv x + \mathrm{i}y$ filled by the infinite depth fluid and a lower complex half-plane (from now on, denoted by $\mathbb{C}^-$) of a variable $w \equiv u + \mathrm{i}v$ (see Fig. 1). The real line $v = 0$ is mapped into the free surface by $z(w)$ being the analytic function in the lower half-plane of w as well as the complex fluid velocity potential $\Pi(w)$ is also analytic in $\mathbb{C}^-$. Both $z(w)$ and $\Pi(w)$ have singularities in upper half-plane (here and further denoted by $\mathbb{C}^+$).

The knowledge of singularities in $\mathbb{C}^+$ would result in the efficient description of the solution in the physical variables. Examples of such type of solutions in hydrodynamic-type systems are numerous including, e.g., the dynamics of free surface of ideal fluid with infinite depth [26–28] and finite depth [29], dynamics of interface between two ideal fluids [27], ideal fluid pushed through viscous fluid in a narrow gap between two parallel plates (Hele–Shaw flow) [30], and the dynamics of the interface between ideal fluid and light viscous fluid [31] and bubble pinch-off [32]. In these systems, the dynamics is determined by poles/branch cuts in the complex plane. Related systems correspond to the spontaneous

appearance of curvature singularities on vortex sheets as obtained in [33]. Nie and Baker (1998) established that Moore's singularities are present in axisymmetric vortex sheets. Authors in [34] considered cone-shaped nose of $2\pi/3$ degrees in axisymmetric flow. Ishihara and Kaneda (1994) and Hou and Hu (2003) extended Moore's singularities to three-dimensional (3D) vortex sheets. Opposite limit is the global existence of water waves for small enough data shown both for 2D [35] and 3D [36] flows.

In this paper, we determine that for Stokes wave the only singularities in $\mathbb{C}^+$ of both $z(w)$ and $\Pi(w)$ are the square-root branch points located periodically at $w = n\lambda + \mathrm{i}v_c - ct$, $n = 0, \pm 1, \pm 2, \ldots$ (we choose the crests of Stokes wave to be located at $w = n\lambda - ct$), and we determine v_c numerically as a function of H/λ. Here, c is the velocity of propagation of Stokes wave which depends on H. To address these singularities, we performed high- precision simulations (both a quad precision of 32 digits accuracy and a variable precision of 200 digits accuracy were used) of Stokes wave ranging from near-linear Stokes wave with $H/\lambda \to 0$, $c \to 1$, and $v_c/\lambda \gg 1$ to near-limiting Stokes wave with $v_c/\lambda \simeq 10^{-7}$ and $H \to H_{max}$. In the previous work [37], we found that as $H \to H_{max}$, the branch point approaches real axis with the scaling law

$$v_c \propto (H_{max} - H)^{\delta}, \tag{1}$$

where $\delta = 1.48 \pm 0.03$. We also provided an accurate estimation of maximum amplitude of the Stokes wave H_{max}, which is farther improved here. The main result of this paper is that we characterized the complex singularities in the upper complex half-plane by rational Padé interpolants of Stokes wave in the complex plane. In this paper, we understand Padé approximation as the least squares rational approximation [38, 39]. We found that as the number of poles used in Padé approximation increases, their density converges to the continuous jumps across the branch cuts connecting the square-root branch points $w = n\lambda + \mathrm{i}v_c - ct$, $n = 0, \pm 1, \pm 2, \ldots$, and $\mathrm{i}\infty$. We also used the series expansion of the jump along branch cuts near branch points to recover the square-root singularity at the branch point. In addition, we provided tables of Padé approximations that allow to easily reproduce our numerically obtained Stokes wave with the relative accuracy of at least 10^{-26}.

The paper is organized as follows. In Section 2, we introduce the basic equations of 2D hydrodynamics in conformal variables and reduce these equations to the equation for Stokes wave. In Section 3, numerical approaches to simulation of Stokes wave are given together with the results of simulations. Also, numerical procedures to recover the location and type of the branch point are discussed. Section 4 introduces a new variable ζ defining a second conformal transformation that maps one spatial period of Stokes wave into the entire real line. Then the Padé approximation

of Stokes wave is found in complex ζ plane. The efficient Alpert–Greengard–Hagstrom (AGH) algorithm [38, 39] is used to obtain the Padé approximation. That algorithm allows to avoid the appearance of artificial zeros and poles of Padé approximation and achieves a spectral accuracy. The convergence of the Padé approximation to the branch cut singularity is established that allows to recover the jump at branch cut. Section 5 studies the jump at the branch cut and shows how to use the series expansion of the jump along branch cuts to address the square-root singularity at the branch point. It is demonstrated that there are no more singularities in the finite complex plane beyond one branch point $w = \mathrm{i}v_c$ per period. In Section 6, the main results of the paper are discussed. Appendix A provides a derivation of basic hydrodynamic equations in conformal variables. Appendix B gives a short description of AGH algorithm adapted for Stokes wave. Appendix C describes a notation used for the tables of Padé approximants for Stokes wave and gives samples of such tables. These tables reproduce the Stokes wave with the relative accuracy of at least 10^{-26}.

2. Basic equations

In physical coordinates (x, y), a velocity $\mathbf{v}$ of $2D$ potential flow of inviscid incompressible fluid is determined by a velocity potential $\Phi(x, y, t)$ as $\mathbf{v} = \nabla\Phi$. The incompressibility condition $\nabla \cdot \mathbf{v} = 0$ results in the Laplace equation

$$\nabla^2\Phi = 0 \tag{2}$$

inside fluid $-\infty < y < \eta(x, t)$. To obtain the closed set of equations, we add the decaying boundary condition at large depth $\Phi(x, y, t)|_{y\to-\infty} = 0$, the kinematic boundary condition

$$\frac{\partial\eta}{\partial t} = \left(-\frac{\partial\eta}{\partial x}\frac{\partial\Phi}{\partial x} + \frac{\partial\Phi}{\partial y}\right)\Bigg|_{y=\eta(x,t)} \tag{3}$$

and the dynamic boundary condition

$$\left(\frac{\partial\Phi}{\partial t} + \frac{1}{2}(\nabla\Phi)^2\right)\Bigg|_{y=\eta(x,t)} + g\eta = 0 \tag{4}$$

at the free surface

$$y = \eta(x, t). \tag{5}$$

We define the boundary value of the velocity potential as

$$\Phi(x, y, t)|_{y=\eta(x,t)} \equiv \psi(x, t). \tag{6}$$

Consider a time-dependent conformal transformation

$$z = z(w, t), \quad w = u + iv. \tag{7}$$

In the remaining part of this section, we use the transformation (7) to reduce the solution of the closed system of Eqs. (2)–(5) into the equivalent set of two equations for z and ψ. After that, we make the reduction to the Stokes wave solution.

We choose the time-dependent conformal transformation (7) in such a way that it maps a half-strip $-\frac{\lambda}{2} \le u < \frac{\lambda}{2},\ -\infty < v \le 0$ of complex plane w into a region $-\frac{\lambda}{2} \le x < \frac{\lambda}{2},\ -\infty < y \le \eta(x, t)$ of complex physical plane $z = x + \mathrm{i}y$ at each time t such that the line segment $-\frac{\lambda}{2} \le u < \frac{\lambda}{2},\ v = 0$ is mapped into a line of free surface $x + \mathrm{i}\eta(x, t)$ with $-\frac{\lambda}{2} \le x < \frac{\lambda}{2}$ and

$$x\left(-\frac{\lambda}{2}\right) = -\frac{\lambda}{2}, \quad x\left(\frac{\lambda}{2}\right) = \frac{\lambda}{2}. \tag{8}$$

Also, $w = -\mathrm{i}\infty$ maps into $z = -\mathrm{i}\infty$. Here, the flow is assumed to be periodic in the horizontal direction with the period λ both in w and z variables. Conditions (8) suggest to separate $z(w, t)$ into a periodic part $\tilde{z}(w, t)$ and a nonperiodic part w as follows:

$$z(w, t) = w + \tilde{z}(w, t), \text{ or } x(w, t) = u + \tilde{x}(w, t), \quad y(w, t) = v + \tilde{y}(w, t), \tag{9}$$

where

$$\tilde{z}(w + \lambda) = \tilde{z}(w), \quad \tilde{x}\left(\pm\frac{\lambda}{2}\right) = 0. \tag{10}$$

Equations (9) and (10) extend conformal transformation (7) into $\mathbb{C}^-$. Also, $x(u, t)$ and $y(u, t)$ form a parametric representation (over the parameter u) of the free surface elevation (5).

The idea of using time-dependent conformal transformation for unsteady fluid flow was exploited by several authors including [13, 26, 40–43]. We follow [42] to recast the system (2)–(4) into the equivalent form for $x(u, t)$, $y(u, t)$, and $\psi(u, t)$ at the real line $w = u$ of the complex plane w using the conformal transformation (7) (see Appendix A for more details). A kinematic boundary condition (3) is reduced to

$$y_t x_u - x_t y_u + \hat{H}\psi_u = 0, \tag{11}$$

and the dynamic boundary condition (4) is given by

$$\psi_t y_u - \psi_u y_t + g y y_u = -\hat{H}\left(\psi_t x_u - \psi_u x_t + g y x_u\right), \tag{12}$$

where $x(u, t)$ is expressed through $y(u, t)$ as follows:

$$\tilde{x} = x - u = -\hat{H}y, \tag{13}$$

(see Eq. (31) below and discussion after it for the justification of that expression) and

$$\hat{H}f(u) = \frac{1}{\pi}\text{p.v.}\int_{-\infty}^{+\infty}\frac{f(u')}{u'-u}\mathrm{d}u' \tag{14}$$

is the Hilbert transform with p.v. meaning a Cauchy principal value of integral. Periodicity of $f(u)$ allows to reduce the integration in the Hilbert transform as follows:

$$\begin{aligned}\hat{H}f(u) &= \frac{1}{\pi}\sum_{n=-\infty}^{\infty}\text{p.v.}\int_{-\lambda/2}^{\lambda/2}\frac{f(u')}{u'-u+n\lambda}\mathrm{d}u' \\ &= \frac{1}{\lambda}\text{p.v.}\int_{-\lambda/2}^{\lambda/2}\frac{f(u')}{\tan\left(\pi\frac{u'-u}{\lambda}\right)}\mathrm{d}u'.\end{aligned} \tag{15}$$

Also in Eqs. (11) and (12) and all subsequent equations, the subscripts mean partial derivatives, e.g., $x_t = \frac{\partial}{\partial t}x$, $x_u = \frac{\partial}{\partial u}x$, etc.

The equivalence of Eqs. (11) and (12) to Eqs. (2)–(4) uses the analyticity of $z(w)$ and $\Pi(w)$ in $\mathbb{C}^-$, where

$$\Pi = \Phi + \mathrm{i}\Theta \tag{16}$$

is the complex velocity potential. Here, Θ is the stream function defined by $\Theta_x = -\Phi_y$ and $\Theta_y = \Phi_x$ to satisfy Cauchy–Riemann conditions for analyticity of $\Pi(z,t)$ in z plane. The conformal transformation (7) ensures that

$$\Theta_u = -\Phi_v, \quad \Theta_v = \Phi_u \tag{17}$$

in w plane. The periodicity of the flow implies the condition

$$\Pi(w+\lambda,t) = \Pi(w,t) \tag{18}$$

together with Eq. (10). We also assumed in Eqs. (11) and (12) that

$$\int_{-\lambda/2}^{\lambda/2}\eta(x,t)\mathrm{d}x = \int_{-\lambda/2}^{\lambda/2}y(u,t)x_u(u,t)\mathrm{d}u = 0, \tag{19}$$

where Eq. (5) was used. Equation (19) states that the mean elevation of free surface is set to zero. Equation (19) is valid at all times and reflects a conservation of the total mass of fluid.

Both Eqs. (11) and (12) are defined on the real line $w = u$. The Hilbert operator $\hat{H}$ transforms into the multiplication operator

$$(\hat{H}f)_k = \mathrm{i}\,\mathrm{sign}\,(k)\,f_k, \tag{20}$$

for the Fourier coefficients (harmonics) f_k,

$$f_k = \frac{1}{\lambda}\int_{-\lambda/2}^{\lambda/2} f(u)\exp\left(-\mathrm{i}ku\frac{2\pi}{\lambda}\right)\mathrm{d}u, \tag{21}$$

of the periodic function $f(u) = f(u+\lambda)$ represented through the Fourier series

$$f(u) = \sum_{k=-\infty}^{\infty} f_k \exp\left(\mathrm{i}ku\frac{2\pi}{\lambda}\right). \tag{22}$$

Here, $\mathrm{sign}(k) = -1, 0, 1$ for $k < 0$, $k = 0$, and $k > 0$, respectively.

The Fourier series (22) allows to rewrite $f(u) = f(w)|_{v=0}$ as follows:

$$f(u) = f^+(u) + f^-(u) + f_0, \tag{23}$$

where

$$f^+(w) = \sum_{k=1}^{\infty} f_k \exp\left(\mathrm{i}kw\frac{2\pi}{\lambda}\right) \tag{24}$$

is the analytical function in $\mathbb{C}^+$,

$$f^-(w) = \sum_{k=-\infty}^{-1} f_k \exp\left(\mathrm{i}kw\frac{2\pi}{\lambda}\right) \tag{25}$$

is the analytical function in $\mathbb{C}^-$, and $f_0 = const$ is the zero harmonic of Fourier series (22). In other words, Eq. (23) decomposes $f(u)$ into the sum of functions $f^+(u)$ and $f^-(u)$, which are analytically continued from the real line $w = u$ into $\mathbb{C}^+$ and $\mathbb{C}^-$, respectively. Equations (20), (23), (24), and (25) imply that

$$\hat{H}f(u) = \mathrm{i}[f^+(u) - f^-(u)]. \tag{26}$$

If function $f(w)$ is analytic in $\mathbb{C}^-$, then $\bar{f}(\bar{w})$ is analytic in $\mathbb{C}^+$ as follows from Eqs. (23)–(25), where bar mean complex conjugation, $\bar{w} = u - \mathrm{i}v$. Then the function $\bar{f}(u)$, $u \in \mathbb{R}$, has analytic continuation into $\mathbb{C}^+$ because at the real line $w = \bar{w}$. Using Eqs. (6) and (16), we obtain that $\psi(u,t) = \frac{1}{2}[\Pi(u,t) + \bar{\Pi}(u,t)]$. It means that after solving Eqs. (11) and (12), one can recover the complex potential Π from the analytical continuation of

$$\Pi(u,t) = 2\hat{P}\psi(u,t) \tag{27}$$

into $\mathbb{C}^-$. Here,

$$\hat{P} = \frac{1}{2}(1 + \mathrm{i}\hat{H}) \tag{28}$$

is the projector operator, $\hat{P}f = f^- + \frac{f_0}{2}$, into a function which has analytical continuation from the real line $w = u$ into $\mathbb{C}^-$, as follows from Eq. (26). Note that without loss of generality, we assumed the vanishing zero Fourier harmonic, $\Pi_0 = 0$, for $\Pi(u, t)$.

Also,

$$\hat{H}^2 f = -f \tag{29}$$

for the function $f(u)$ defined by (23) provided that the additional restriction that $f_0 = 0$ holds. In other words, the Hilbert transformation is invertible on the class of functions represented by their Fourier series provided that zeroth Fourier harmonic f_0 vanishes. If $f_0 \neq 0$, then the identity (29) is replaced by

$$\hat{H}^2 f = -(f - f_0). \tag{30}$$

The analyticity of $z(w)$ in $\mathbb{C}^-$ implies, together with $\tilde{x} = \frac{1}{2}(\tilde{z} + \bar{\tilde{z}})$, $\tilde{y} = \frac{1}{2\mathrm{i}}(\tilde{z} - \bar{\tilde{z}})$, and Eqs. (26) and (30), that at the real line $w = u$ the following relations hold

$$y - y_0 = \hat{H}\tilde{x} \quad \text{and} \quad \tilde{x} - x_0 = -\hat{H}y. \tag{31}$$

Here, x_0 and y_0 are zero Fourier harmonics of $\tilde{x}(u, t)$ and $y(u, t)$, respectively. Also, it follows from Eq. (9) that $y = \tilde{y}$ on the real line $w = u$, thus below we use y notation only. Note that the addition of zero harmonics x_0 and y_0 into Eq. (31) is the modification compared with [42,43]. These Refs. were focused on the decaying boundary conditions $\eta(x, t) \to 0$ and $\psi(x, t) \to 0$ for $|x| \to \infty$ which imply, together with the condition (19) in the limit $\lambda \to \infty$, that $x_0 = y_0 = 0$. However, generally, x_0 and y_0 might be nonzero for the periodic solutions with a finite λ considered in this paper. Both x_0 and y_0 must be time-independent to ensure that the fluid is at rest for $v \to -\infty$ (in the depth of the fluid), in other words, the center of mass of fluid is at rest. By shifting the system in the horizontal direction, one can set without the loss of generality that $x_0 = 0$. Then, Eq. (31) results in Eq. (13).

Equations (31) imply that it is enough to find either $y(u, t)$ or $x(u, t)$, then the second of them is recovered by these explicit expressions. Taking the derivative of Eqs. (31) with respect to u results in the similar relations

$$y_u = \hat{H}\tilde{x}_u \quad \text{and} \quad \tilde{x}_u = -\hat{H}y_u. \tag{32}$$

2.1. Progressive waves

Stokes wave corresponds to a solution of the system (11) and (12) in the traveling wave form

$$\psi(u, t) = \psi(u - ct), \ \tilde{z}(u, t) = \tilde{z}(u - ct), \tag{33}$$

where both ψ and $\tilde{z}$ are the periodic functions of $u - ct$. Here, c is the phase velocity of Stokes wave. We transform into the moving frame of reference, $u - ct \to u$, and assume that the crest of the Stokes wave is located at $u = 0$ as in Fig. 1, and λ is the spatial period in u variable for both ψ and $\tilde{z}$ in Eqs. (33). We look for the Stokes wave that has one crest per period. Higher order progressive waves are also possible, which have more than one different peak per period [44]. However, here, we consider only Stokes wave. We recall that the spatial period λ is the same in both u and x variables as follows from Eq. (10). In addition, it implies that the phase velocity is the same both in u and x variables so that the Stokes wave has the moving surface $y = \eta(x - ct)$ and the velocity potential $\psi = \psi(x - ct)$ in physical spatial variables (x, y) with the same value of c as in Eqs. (33). To understand that we notice that if it would be different velocity c in x and $\tilde{c}$ in u variable so that Eqs. (33) had the argument $u - \tilde{c}t$, then the same spatial period in both x and u variables given by Eq. (8) would immediately imply that $\tilde{c} = c$. The Stokes solution requires $y(u)$ to be the even function, while $\tilde{x}(u)$ needs to be the odd function, which ensures that $y = \eta(x - ct)$ is the even function. See also Appendix B of Part II [45] for more discussion on that.

It follows from (11) and (33) (corresponding to substitution $\frac{\partial}{\partial t} \to -c\frac{\partial}{\partial u}$ for y and ψ and $\frac{\partial x}{\partial t} \to -c\frac{\partial \tilde{x}}{\partial u}$) that

$$\hat{H}\psi_u = cy_u. \tag{34}$$

Also, Eq. (12) turns under the same substitution into

$$gyy_u = -\hat{H}\left(-c\psi_u + gyx_u\right). \tag{35}$$

Using Eq. (34) to excluding ψ_u from Eq. (35), we obtain that

$$-c^2 y_u + gyy_u + g\hat{H}[y(1 + \tilde{x}_u)] = 0. \tag{36}$$

We now apply $\hat{H}$ to (36), use (31) to obtain a closed expression for y, and introduce the operator $\hat{k} \equiv -\partial_u \hat{H} = \sqrt{-\nabla^2}$, which results in the following expression

$$\hat{L}_0 y \equiv (c^2\hat{k} - 1)y - \left(\frac{\hat{k}y^2}{2} + y\hat{k}y\right) = 0, \tag{37}$$

where we made all quantities dimensionless by the following scaling transform $u \to u\lambda/2\pi$, $x \to x\lambda/2\pi$, $y \to y\lambda/2\pi$, and c is scaled by c_0 as follows $c \to c\,c_0$, where $c_0 = \sqrt{g/k_0}$ is the phase speed of linear gravity wave with the wavenumber $k_0 = 2\pi/\lambda$. In these scaled units, the period of ψ and $\tilde{z}$ is 2π. Our new operator $\hat{k}$ in Fourier space acts as multiplication operator, qualitatively similar to $\hat{H}$: $(\hat{k}f)_k = kf_k$.

3. Numerical simulation of Stokes wave

We solve Eq. (37) numerically to find $y(u)$ by two different methods each of them beneficial for different ranges of the parameter H/λ. For both methods, $y(u)$ was expanded in cosine Fourier series, and the operator $\hat{k}$ was evaluated numerically using fast Fourier transform (FFT). A uniform grid with M points was used for the discretization of $-\pi \le u < \pi$. A first method is inspired by a Petviashvili method [46], which was originally proposed to find solitons in nonlinear Schrödinger (NLS) equation, as well as it was adapted for nonlocal NLS-type equations, see, e.g. [47]. We used a version generalized Petviashvili method (GPM) [48, 49] adjusted to Stokes wave as described in [37]. In practice, this method allowed to find high-precision solutions up to $H/\lambda \lesssim 0.1388$. The performance of that method for larger values of H/λ was limited by the decrease in the speed of numerical convergence.

3.1. Newton CG and newton CR methods

The convergence of GPM can be accelerated by the method of Ref. [50]. We tried that method for Eq. (37), but the acceleration was only moderate while we encountered fast growing computation times when increased H/λ. Instead for larger H/λ, we used a second method which is the Newton conjugate gradient (Newton-CG) method proposed in [51, 52]. We found that method to be far superior than GPM, which agrees with the conclusion of Ref. [53]. We were solving Eq. (37) by gradually changing the parameter c and used the solution for previous value of c as an initial approximation. It allowed to use Newton-CG method immediately without initial stage of finding solution with $1-10\%$ accuracy by GPM as proposed in Ref. [53].

The idea behind the Newton-CG method is to first linearize Eq. (37) about the current nth approximation $y^{(n)}$, assuming that the exact solution y with $\hat{L}_0 y = 0$ can be written as a sum of current approximation and a correction $\delta y^{(n)}$ such that $y = y^{(n)} + \delta y^{(n)}$. Then, $\hat{L}_0 y^{(n)} + \hat{L}_1 y^{(n)} \simeq 0$, where $\hat{L}_1 = -\hat{M}\delta y^{(n)} - (\hat{k}(y^{(n)}\delta y^{(n)}) + y^{(n)}\hat{k}\delta y^{(n)} + \delta y^{(n)}\hat{k}y^{(n)})$ is the linearization of $\hat{L}_0$ around the current approximation $y^{(n)}$ and $\hat{M} \equiv -c^2\hat{k} + 1$. Second, solve the resulting linear system $\hat{L}_1 \delta y_n = -\hat{L}_0 y_n$ for δy_n with one of numerical linear algebra methods, in our case it was either conjugate gradient (CG) method [54] or conjugate residual (CR) method [55] to obtain next approximation $y^{(n+1)} = y^{(n)} + \delta y$. It should be noted that monotonic convergence of CG or CR methods was proven only for positive definite (semidefinite for CR) operators, while in our case $\hat{L}_1$ is indefinite. Nevertheless, both methods were converging (although generally nonmonotonically) to the solutions, and convergence was much faster than using GPM.

Newton-CG/CR methods can be written in either Fourier space, or in physical space. We considered both cases, however, Newton-CG/CR methods in Fourier space require four FFTs per CG/CR step, while in physical space it requires at least six. For both cases, CG and CR, we used $\hat{M}$ as a preconditioner. Singularities of the operator $\hat{M}^{-1} = (-c^2|k| + 1)^{-1}$ are avoided in our simulations because the wavenumber $|k|$ is integer, while for any Stokes wave c is within the range $1 < c^2 < 1.3$. We found that the region of convergence of the Newton-CG/CR methods to nontrivial physical solution (37) is relatively (with respect to GPM) narrow and requires an initial guess $y^{(0)}$ to be quite close to the exact solution y. In practice, we first run GPM and then choose $y^{(0)}$ for Newton-CG/CR methods as the last available iterate of GPM.

Because most of our interest was in getting the dependence of characteristics of Stokes waves on the wave height and the only parameter in Eq. (37) is velocity of propagation c, we were calculating waves changing continuously the parameter c and using results of computations with previous values of c as initial condition $y^{(0)}$ for the Newton-CG/CR iterations. Due to this approach, Newton-CG/CR methods converge to the nontrivial solution in all cases provided that we additionally used the numerical procedure described below in Section 3.2.

3.2. Stokes wave velocity as a function of steepness

Results of multiple simulations of Stokes wave are shown in Fig. 2, where the wave velocity c is shown as a function of the dimensionless wave height H/λ. This function is nonmonotonic in agreement with previous simulations [8, 11, 12] and theoretical analysis [9, 10], which predicted an infinite number of oscillations.

It might be also beneficial to apply imaginary-time evolution method with amplitude normalization described in Ref. [56] because potentially it might allow to vary the H/λ directly and adjust c afterward to match each given value of H/λ. That would allow to avoid the difficulty with the nonmonotonicity of c-dependence. This method is, however, beyond the scope of this paper.

We were able to resolve with quadruple precision two oscillations (two maxima and one nontrivial minimum) of the propagation velocity as a function of H/λ. These oscillations represent a challenge for simulation, because propagation velocity is the only parameter in Eq. (37). Thus, it is impossible to go over the first maximum by changing continuously velocity of propagation c. This is because after the maximum is reached, we have to start decreasing the parameter c. However, decreasing of c causes iterations to converge to the less steep solution on the left from the maximum (which

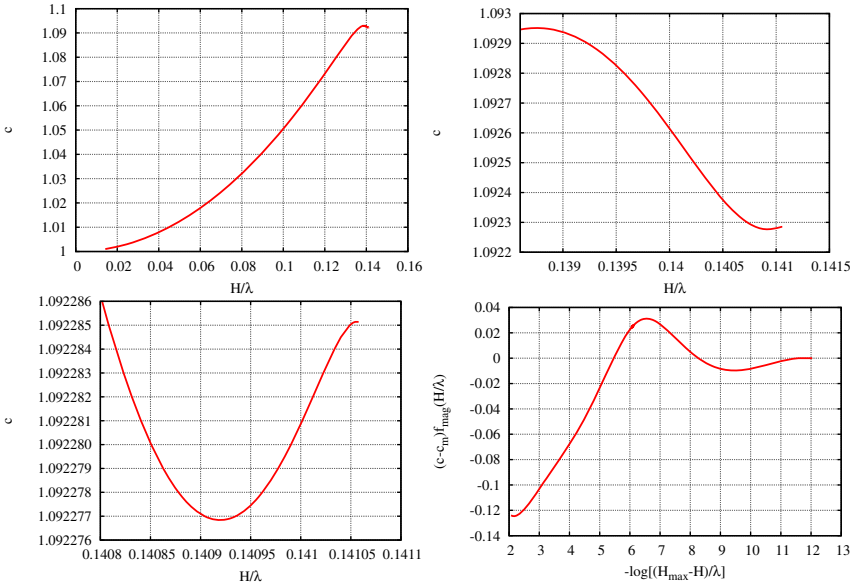

Figure 2. Oscillations of dimensionless velocity of Stokes wave propagation as a function of steepness obtained from simulations. First three plots from left to right and from top to bottom have increasing zoom both in vertical and horizontal axes to focus on oscillations. In the lower right corner, a plot is scaled by a magnification function $f_{mag}(H/\lambda) = 1/(30(H_{max} - H)/\lambda)^{1.15} + 1$ to show all simulation data in a single graph while stressing obtained oscillations.

we already obtained on previous steps), instead of steeper solutions to the right from the maximum.

To resolve this issue, we used the following approach. Assume that the singularity of $\tilde{z}$ closest to real axis in w complex plane is the branch point

$$\tilde{z} \simeq c_1(w - \mathrm{i}v_c)^{\beta} \tag{38}$$

for $w \to \mathrm{i}v_c$, where c_1 is the complex constant, $v_c > 0$, and β are real constants. By the periodicity in u, similar branch points are located at $w = \mathrm{i}v_c + 2\pi n$, $n = \pm 1, \pm 2, \ldots$ (recall that we already switched to the dimensionless coordinates). We expand $\tilde{z}(u)$ into Fourier series $\tilde{z}(u) = \sum_{-\infty}^{k=0} \hat{\tilde{z}}_k \exp(\mathrm{i}ku)$, where

$$\hat{\tilde{z}}_k = \frac{1}{2\pi} \int_{-\pi}^{\pi} \tilde{z}(u) \mathrm{e}^{-\mathrm{i}ku} \mathrm{d}u \tag{39}$$

are Fourier coefficients, and the sum is taken over nonpositive integer values of k, which ensures both 2π-periodicity of $\tilde{z}(u)$ and analyticity of $\tilde{z}(w)$ in $\mathbb{C}^-$. We evaluate (39) in the limit $k \to -\infty$ by moving the integration

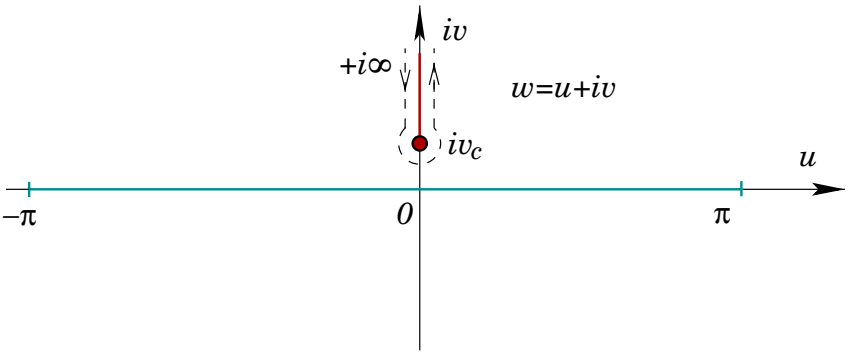

Figure 3. Schematic of contour in the $\mathbb{C}^+$ which allows to determine distance v_c from the branch cut to the real axis.

contour from the line $-\pi < u < \pi$ into $\mathbb{C}^+$ until it hits the lowest branch point (38), thus it goes around branch point and continues straight upward about both sides of the corresponding branch cut as shown by the dashed line of Fig. 3. Here, we assume that branch cut is a straight line connecting $w = \mathrm{i}v_c$ and $+\mathrm{i}\infty$. Then, the asymptotic of $|\hat{\tilde{z}}_k|$ is given by [37]

$$|\hat{\tilde{z}}_k| \propto |k|^{-1-\beta} e^{-|k|v_c}, \quad k \to -\infty. \tag{40}$$

This approach was used in our previous work [37] to evaluate distance v_c of the lowest singularity to the real line. Now, our key idea is to push artificially the singularity $w = iv_c$ toward the real line, thus increasing H/λ. It follows from expression (40) that to decrease v_c, we can multiply Fourier coefficients of the previously obtained Stokes wave solution $\hat{\tilde{z}}_k$ by $\exp(\alpha k)$, where the numerical parameter α is chosen such that $0 < \alpha \ll v_c$. The result of this multiplication $\hat{\tilde{z}}_k \exp(\alpha k)$ is not a Stokes wave solution anymore, but it has higher steepness and not very distinct from the Stokes wave solution if α is small enough. After that modification, we slightly decrease c from previous value and allow iterations of Section 3.1 to converge starting from $\hat{\tilde{z}}_k \exp(\alpha k)$ as zero iteration. As we expected, iterations then converge to the solution on the right from the maximum. This procedure allowed us to resolve both maxima and one nontrivial minimum of c as a function of H/λ as summarized in Fig. 2.

3.3. Recovering v_c from the Fourier spectrum of Stokes wave

To obtain the location of the branch point $w = iv_c$ with good precision, one has to go beyond the leading order asymptotic (40). Next order corrections to the integral (39) for $\beta = 1/2$ have the following form:

$$|\hat{\tilde{z}}_k| \simeq \left(c_1|k|^{-3/2} + c_2|k|^{-5/2} + c_3|k|^{-7/2} + c_4|k|^{-9/2}\right.$$

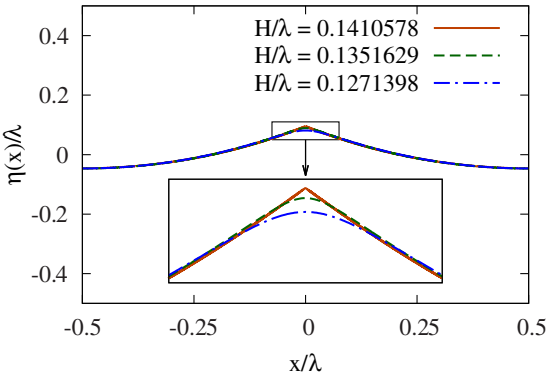

Figure 4. Stokes wave with $c = 1.082$ (blue dash-dotted line), $c = 1.091$ (green dashed line), and $c = 1.0922851405$ (dark orange solid line). Corresponding values of H/λ are given in the legend. Inset shows zoom-in into small values of x/λ near a wave crest.

$$+ \ldots)e^{-|k|v_c}, \quad k \to -\infty, \tag{41}$$

where we took into account the expansion of $\tilde{z}(w)$ in half-integer powers $(w - \mathrm{i}v_c)^{1/2+n}$, $n = 0, 1, 2, \ldots$ beyond the leading order term (38).

The numerically obtained spectrum $|\hat{\tilde{z}}_k|$ of Stokes wave was fitted to the expansion (41) to recover v_c and coefficients c_1, c_2, $c_3, \ldots$. The highest accuracy in recovering v_c was achieved when the middle of spectrum $k \sim k_{max}/2$ was used for that fit, here, $k_{max} = M/2$ is the highest Fourier harmonic used in simulations. $k_{max}/2$ represents a compromise between the highest desired values of k to be as close as possible to asymptotic regime $k \to \infty$ and the loss of numerical precision for $k \to k_{max}$. We estimated the accuracy of the fit by varying values of k used for fitting as well as changing the number of terms in the expansion (41). Typically, we used four terms in (41). Section 4.3 discusses the comparison of the accuracy of the obtained results with the other methods we used to find v_c.

3.4. Highest wave obtained

We calculated $\tilde{z}(u)$ with high accuracy for different values of H/λ using computations in quad precision (32 digits). Such a high precision is necessary to reveal the structure of singularities in $\mathbb{C}^+$. Figure 4 shows the spatial profiles of Stokes waves for several values of H/λ in physical variables (x, y). The Stokes wave quickly approaches the profile of limiting wave except a small neighborhood of the crest.

As it was shown in the previous paper [37], tails of the spectra have asymptotic behavior corresponding to $\beta = 1/2$ in (40), which means that we have square-root branch cut singularity in $\mathbb{C}^+$ all the time. This is consistent with theoretical predictions in [7] and [13].

The number of Fourier modes $M \equiv 2k_{max}$, that we used in FFT (in simulations, we expand $y(u)$ in cosine Fourier series to speed up simulations and to be memory efficient) for each value of H/λ, increases quickly with the increase in H as v_c decreases. E.g., for $H/\lambda = 0.0994457$, it was more than enough to use 256 modes, while for

$$H_{max}^{lowerbound}/\lambda = 0.14105777885488320816492860225695 6 \qquad (42)$$

we used $M = 2^{27} \approx 134 \times 10^6$ modes which corresponds to the largest wave height achieved in our simulations. Due to such high number of modes, the precision of value (42) decreases by round-off errors in approximately $M^{1/2}$ times ($M^{1/2}$ results from the sum of round-off errors of M harmonics of Fourier series), i.e., in ~ 4 digits. This extreme case has $c = 1.0922851405$ (this is the exact number, in simulations, we added zeros beyond these digits to match the number of significant digits for each numerical precision used) and $v_c = 5.938244198928032717 79 \times 10^{-7}$. These numbers are the moderate extension of our previous work [37] by pushing down a lowest value of v_c more than twice. Thus, Eq. (42) provides the best lower bound $H_{max}^{lowerbound}/\lambda$ for the limiting Stokes wave value H_{max}/λ, which we achieved in our simulations. Further decrease in the numerical values of v_c (and increase in $H_{max}^{lowerbound}/\lambda$) can be achieved by both subtracting the leading order singularity (38) from the numerical solution and using the nonuniform numerical grid in u, which concentrates near $u = 0$. These numerical approaches are, however, beyond the scope of this paper.

Before our work [37], the numerical estimates of H_{max} were found in [12] as $H_{max}^{Williams}/\lambda = 0.141063$ and [57] $H_{max}^{GL}/\lambda = 0.14106348398$. The other commonly used but less precise estimate is $H_{max}^{Schwartz}/\lambda = 0.1412$ [8]. It was shown in [37] that numerical values of v_c in the limit $(H_{max} - H)/\lambda \ll 0$ were fitted to the scaling law (1) with

$$H_{max}/\lambda = 0.1410633 \pm 4 \cdot 10^{-7}. \qquad (43)$$

The mean-square error for δ in (1) is $\simeq 0.04$, which offers the exact value $\delta = 3/2$ as a probable candidate for (1). The estimate (43) suggests that the previous estimate $H_{max}^{Williams}$ is more accurate than $H_{max}^{Schwartz}$. Also, H_{max}^{GL} is within the accuracy of the estimate (43). However, H_{max}^{GL} is obtained in [57] from the Michell's expansion [3] of the limiting Stokes wave, which ignores the expansion in powers of the irrational number $\mu = 1.46934574\ldots$ found in Ref. [7]. Existence of that expansion beyond the Stokes 2/3 power law $u^{2/3}$ was established in [7]. Lack of resolving that expansion suggests that H_{max}^{GL} does not have a well-controlled accuracy. In contrast, our numerical results are based on Fourier series for nonlimiting Stokes wave that has well-controlled precision. The difference between (43) and the new lower boundary estimate (42) of the largest H is $\simeq 0.004\%$.

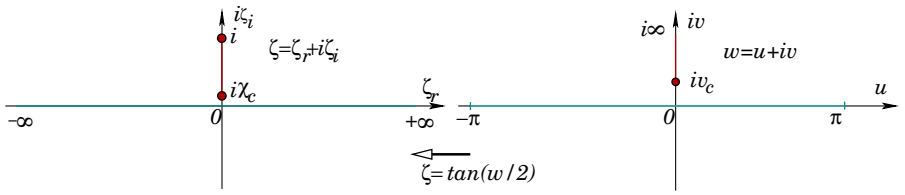

Figure 5. Schematic of a second conformal map between the periodic domain in w-plane (right panel) into $\zeta = \tan(w/2)$-plane. Another useful property of this map is representation of 2π-periodic branch cut from $\mathrm{i}v_c$ to $\mathrm{i}\infty$ as a finite length cut from $\chi_c = \tan(\mathrm{i}v_c/2)$ to i.

4. Padé approximation of Stokes wave

4.1. Additional conformal transformation and spectral convergence of Padé approximation

To analyze the structure of singularities of Stokes wave, we perform an additional conformal transformation between the complex plane $w = u + \mathrm{i}v$ and the complex plane for the new variable

$$\zeta = \tan\left(\frac{w}{2}\right). \tag{44}$$

Equation (44) maps the strip $-\pi < Re(w) < \pi$ into the complex ζ plane. In particular, the line segment $-\pi < w < \pi$ of the real line $w = u$ maps into the real line $(-\infty, \infty)$ in the complex plane ζ as shown in Fig. 5. Vertical half-lines $w = \pm\pi + \mathrm{i}v,\ 0 < v < \infty$ are mapped into a branch cut $\mathrm{i} < \zeta < \mathrm{i}\infty$. In a similar way, vertical half-lines $w = \pm\pi + \mathrm{i}v,\ -\infty < v < 0$ are mapped into a branch cut $-\mathrm{i}\infty < \zeta < -\mathrm{i}$. However, $2\pi-$periodicity of $\tilde{z}(w)$ (10) allows to ignore these two branch cuts because $\tilde{z}(w)$ is continuous across them. Complex infinities $w = \pm\mathrm{i}\infty$ are mapped into $\zeta = \pm\mathrm{i}$. An unbounded interval $[\mathrm{i}v_c, \mathrm{i}\infty)$, $v_c > 0$, is mapped into a finite interval $[\mathrm{i}\chi_c, \mathrm{i})$ with

$$\chi_c = \tanh\frac{v_c}{2}. \tag{45}$$

The mapping (44) is different from the commonly used (see, e.g. [8, 11, 13]) mapping $\zeta = \exp(-\mathrm{i}w)$ (maps the strip $-\pi \le Re(w) < \pi$ into the unit circle). The advantage of using the mapping (44) is the compactness of the interval $(\mathrm{i}\chi_c, \mathrm{i})$ as mapped from the infinite interval $(\mathrm{i}v_c, \mathrm{i}\infty)$. In contrast, the mapping to the circle leaves the interval $(\mathrm{i}v_c, \mathrm{i}\infty)$ infinite in ζ plane.

We use AGH algorithm [38, 39] to approximate the Stokes wave $\tilde{z}(\zeta)$ at the real line $\mathrm{Re}(\zeta) = \zeta$ by a set of poles in the complex ζ plane. Approximation by a set of poles is a particular case of Padé approximation by rational functions $\frac{P(\zeta)}{Q(\zeta)}$, where $P(\zeta)$ and $Q(\zeta)$ are polynomials. Zeros of $Q(\zeta)$ give the location of poles. Looking at complex values of ζ in

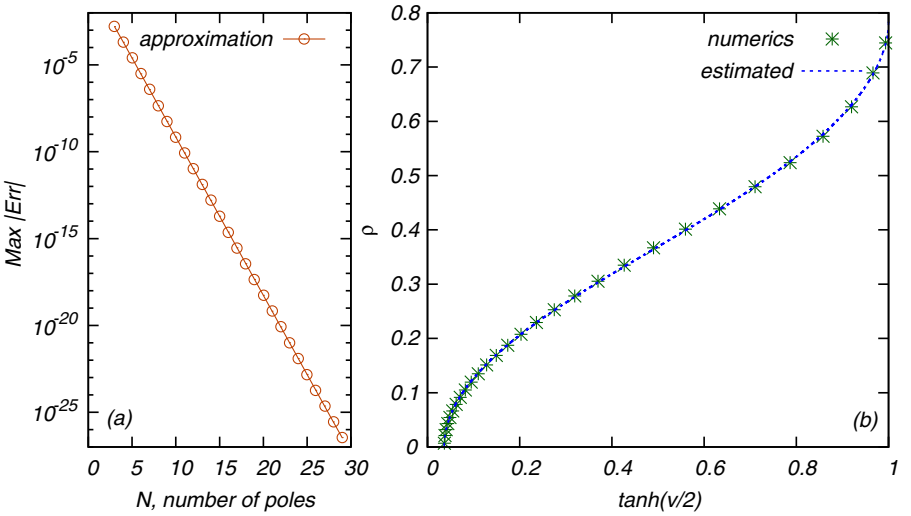

Figure 6. (a) An exponential decay of error in Padé approximation of Stokes for $H/\lambda = 0.12551024766621203511898125908053$ as a function of the number of poles N. (b) The density $\rho(\chi)$ on the branch cut sampled at $\zeta_k = \mathrm{i}\chi_k \equiv \mathrm{i}\tanh(\frac{v_k}{2})$, $k = 1, \ldots, N$, obtained from the Padé approximation of Stokes wave from (a) with $N = 29$ (green stars). Blue-dotted line is the estimated profile of $\rho(\chi)$ for the same Stokes wave in the continuous limit of $N \to \infty$.

the rational function $\frac{P(\zeta)}{Q(\zeta)}$ provides the analytical continuation of $\tilde{z}(\zeta)$ into the complex ζ plane. Usually, Padé approximation is numerically unstable because of the pairs of spurious zeros and poles appear in finite precision arithmetics. These doublets correspond to positions of zeros of $P(\zeta)$ and $Q(\zeta)$, which nearly cancel each other. In our practical realizations, AGH algorithm avoids the numerical instability of the Padé approximation until the number of poles N increases to reach the accuracy corresponding to the round-off error in the numerical approximation of $\tilde{z}(u)$. If the analytical continuation of $\tilde{z}(u)$ into $w \in \mathbb{C}$ has a branch cut, the AGH algorithm places poles along the branch cut. AGH algorithm is outlined in Appendix B.

We applied AGH algorithm for $\tilde{z}(\zeta)$ at the real line $\mathrm{Re}(\zeta) = \zeta$, where $\tilde{z}(\zeta)$ is obtained from simulations described in Section 3. Increasing N, we observed the exponential convergence of Padé approximation $z(\zeta)_{pade}$ to $\tilde{z}(\zeta)$ as

$$err_\infty \propto e^{-p(v_c)N}, \tag{46}$$

where $err_\infty \equiv \max_{-\infty<\zeta<\infty} |\tilde{z}(\zeta) - \tilde{z}(\zeta)_{pade}|$ is the error in infinity (maximum) norm. An example of the exponential convergence is shown in Fig. 6(a) for a particular Stokes wave. Here, $p(v_c)$ is the function of v_c but

is independent of N. We found that with high precision

$$p(v_c) \propto v_c^{1/6}. \tag{47}$$

AGH algorithm is looking for poles in the entire complex plane ζ. All the encountered poles for Stokes wave were found on the interval of imaginary axis along the interval $[\mathrm{i}\chi_c, \mathrm{i})$, where χ_c is determined numerically as in Section 3.

Equations (46) and (47) demonstrate excellent performance of Padé approximation. E.g., decreasing v_c by six order required in our simulations only 10-fold increase in N as detailed in Appendix C. It suggests that numerical method, which solves Stokes wave equation (37) directly in terms of Padé approximants, might be superior to Fourier methods including numerical approaches mentioned in Section 3.3. This topic is, however, beyond the scope of this paper.

It is rather straightforward to distinguish in AGH algorithm poles from branch cuts. If both poles and branch cuts would be present in $\tilde{z}(\zeta)$, then increasing N one observes that some poles of Padé approximation are not moving and their complex residues remain approximately the same. These correspond to poles of $\tilde{z}(\zeta)$. Such a behavior occurs for test problems when we artificially added extra poles to $\tilde{z}(\zeta)$. Other poles of Padé approximation are moving with the increase in N, and their complex residues are changing. These poles mark the spatial location of branch cuts of $\tilde{z}(\zeta)$. The density of poles along each branch cut is increasing with the increase in N. If the jump of $\tilde{z}(\zeta)$ at branch cut is continuous along it, then we expect to see the convergence of density of poles with the increase in N. All this is valid until err_∞ decreases down to the level of round-off error at which $\tilde{z}(\zeta)$ was determined. Further increase in N would result in the appearance of spurious poles at random positions of ζ plane with the magnitudes of complex residues at the level of round-off error ($\sim 10^{-32}$ for $z(\zeta)$ found with quad precision in Section 3).

Using $\tilde{z}(\zeta)$ obtained by the method of Section 3, we found a single branch cut $[\mathrm{i}\chi_c, \mathrm{i})$ but no poles in Stokes wave. It means that in complex w plane, we have one branch cut per spatial period 2π located at $(2\pi n + \mathrm{i}v_c, 2\pi n + \mathrm{i}\infty)$, $n \in \mathbb{N}$.

We parameterize that branch cut as follows:

$$\tilde{z}(\zeta) = \mathrm{i}y_b + \int_{\chi_c}^{1} \frac{\rho(\chi')\mathrm{d}\chi'}{\zeta - \mathrm{i}\chi'}, \tag{48}$$

where $\rho(\chi)$ is the density along branch cut, and $y_b \equiv y(\pi)$ is the minimum height of Stokes wave as a function of x (or in the similar way, as the function of u). That density is related to the jump of $\tilde{z}(\zeta)$ at branch cut

as explained in Section 5.1. The constant y_b is determined by the value of $\tilde{z}(\zeta)|_{\zeta=\infty} = \tilde{z}(w)|_{w=\pi}$. This constant has a zero imaginary part, $\mathrm{Im}(y_b) = 0$, because $\tilde{x}(w)|_{w=\pi/2} = 0$ as given by Eq. (10).

The Padé approximation represents Eq. (48) as follows:

$$\tilde{z}(\zeta) = \mathrm{i}y_b + \int_{\chi_c}^{1} \frac{\rho(\chi')\mathrm{d}\chi'}{\zeta - \mathrm{i}\chi'} \simeq \mathrm{i}y_b + \sum_{n=1}^{N} \frac{\gamma_n}{\zeta - \mathrm{i}\chi_n}, \tag{49}$$

where the numerical values of the pole positions χ_n and the complex residues γ_n ($n = 1, \ldots, N$) are obtained from AGH algorithm.

4.2. Recovering jump along branch cut

We recover $\rho(\chi)$ from Eq. (49) as follows. Assume that we approximate the integral in Eq. (48) by the trapezoidal rule

$$\int_{\chi_c}^{1} \frac{\rho(\chi')\mathrm{d}\chi'}{\zeta - \mathrm{i}\chi'} \simeq \frac{\chi_2 - \chi_1}{2} \frac{\rho_1}{\zeta - \mathrm{i}\chi_1} + \sum_{n=2}^{N-1} \frac{\chi_{n+1} - \chi_{n-1}}{2} \frac{\rho_n}{\zeta - \mathrm{i}\chi_n} + \frac{\chi_N - \chi_{N-1}}{2} \frac{\rho_N}{\zeta - \mathrm{i}\chi_N}. \tag{50}$$

A comparison of Eqs. (49) and (50) suggests the approximation $\rho_{n,N}$ of the density $\rho(\chi_n)$ on the discrete grid χ_n, $n = 1, \ldots, N$ as follows:

$$\rho(\chi_n) \simeq \rho_{n,N} = \frac{2\gamma_n}{\chi_{n+1} - \chi_{n-1}} \quad \text{for} \quad n = 2, \ldots, N-1, \tag{51a}$$

$$\rho(\chi_1) \simeq \rho_{1,N} = \frac{2\gamma_1}{\chi_2 - \chi_1}; \ \rho(\chi_N) \simeq \rho_{N,N} = \frac{2\gamma_N}{\chi_N - \chi_{N-1}}. \tag{51b}$$

A convergence of $\rho_{n,N}$ to the continuous limit $\rho(\chi_n)$ as N increases is quadratic with the error scaling $\propto \frac{1}{N^2}$ for χ away from boundaries $\chi = \chi_c$ and $\chi = 1$. Near these boundaries, we cannot apply the trapezoidal rule and have to resort to less accurate estimates given by Eq. (51b). Figure 6(b) shows the particular example of $\rho(\chi)$ (shown by solid line) compared with $\rho_{n,N}$ (shown by stars) for $N = 29$. Figure 7 demonstrates this $\propto \frac{1}{N^2}$ convergence of the Padé approximation to the continuous limit. We believe that the convergence of ρ_n to the continuous value $\rho(\chi)$ as $N \to \infty$ and absence of other poles outside of $[\mathrm{i}\chi_c, \mathrm{i}]$ provide a numerical proof that the only singularity of $\tilde{z}(\zeta)$ are the branch points $\mathrm{i}\chi_c$ and i connected by the branch cut $\zeta \in [\mathrm{i}\chi_c, \mathrm{i}]$.

At $\chi = \chi_c$, the function $\rho(\chi)$ has a square-root singularity as given below by Eq. (56). This singularity additionally reduces the accuracy of

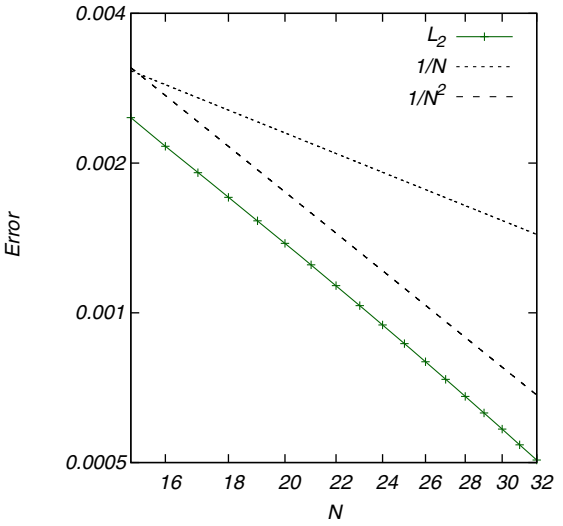

Figure 7. Error between Padé approximation with N poles and the continuous limit for $\rho(\chi)$ for Stokes wave with $H/\lambda = 0.12551024766621203511898125908053$ in log-log scale. It is seen that the error $\propto \frac{1}{N^2}$. To calculate that error, we use a spline interpolation for $\rho^2_{n,N}$ with $N = N_{max} = 216$ to construct the approximation of the continuous limit of the square of the density, $\rho_{continuous}(\chi)$. After that, the error is defined as $\text{err} \equiv (\sum_{n=1}^{N-1}[\rho_{n,N} - \rho_{continuous}(\chi_n)]^2)^{1/2}/(N-1)$ for each N, where $\rho_{n,N}$ are given by Eqs. (51a) and (54). For comparison, dashed and dotted lines show $1/N^2$ and $1/N$ scaling, respectively.

the approximation (51b) for $\rho_{1,N,}$ which is based on Taylor series. To significantly improve the numerical accuracy of $\rho_{1,N,}$ we assume that ρ has the following square-root dependence in the vicinity of χ_c:

$$\rho_{approx}(\chi) = A\sqrt{\chi - \chi_c}. \tag{52}$$

Here, the values of the parameters A and χ_c are determined from two interior points $(\chi_2, \rho_{2,N})$ and $(\chi_3, \rho_{3,N})$ found via the trapezoid rule (51a). We assume that $\rho_{approx}(\chi_2) = \rho_{2,N}$ and $\rho_{approx}(\chi_3) = \rho_{3,N,}$ which gives that

$$A = \left(\frac{\rho^2_{3,N} - \rho^2_{2,N}}{\chi_3 - \chi_2}\right)^{1/2}, \qquad \chi_c = \frac{\rho^2_{3,N}\chi_2 - \rho^2_{2,N}\chi_3}{\rho^2_{3,N} - \rho^2_{2,N}}. \tag{53}$$

Using Eqs. (52) and (53) for $\chi = \chi_1$, we obtain the numerically accurate approximation that

$$\rho_{1,N} = \left(\frac{(\chi_3 - \chi_1)\rho^2_{2,N} - (\chi_2 - \chi_1)\rho^2_{3,N}}{\chi_3 - \chi_2}\right)^{1/2}, \tag{54}$$

where $\rho_{2,N}$ and $\rho_{3,N}$ are given by Eq. (51a).

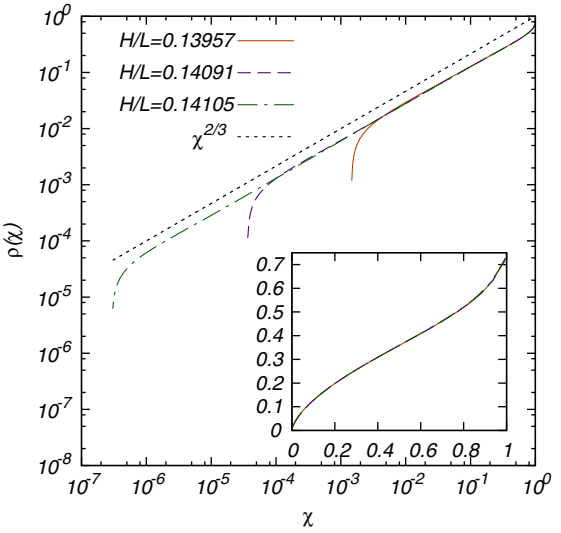

Figure 8. The density $\rho(\chi)$ for three different Stokes waves in log-log scale. A straight dashed line shows $\chi^{2/3}$ scaling law, which corresponds to the limiting Stokes wave. Insert shows $\rho(\chi)$ in linear scale for the same three Stokes waves, which are visually almost indistinguishable.

At $\chi = 1$, the function $\rho(\chi)$ also has singularity and, respectively, numerical value of $\rho_{N,N}$ from (51b) is not very accurate. To improve that accuracy, we use that $\rho(1) = 1$ as found in the accompanying paper Part II [45]. Then using the trapezoidal rule, we obtain more accurate expression that

$$\rho(\chi_N) \simeq \rho_{N,N} = \frac{2\gamma_N}{1 - \chi_{N-1}}. \tag{55}$$

Further improvement of the accuracy of recovering of $\rho(\chi)$ might be possible by using a hybrid Gauss-trapezoidal rule built for a square-root singularity [58]. Such possible improvements are, however, beyond the scope of this paper.

Figure 8 shows the density $\rho(\chi)$ for three different Stokes waves in log-log scaling. It is also seen that inside the branch cut and for small $\chi_c \ll 1$, the density $\rho(\chi)$ scales as $\chi^{2/3}$ which corresponds to the limiting Stokes wave. A deviation from that scaling occurs near $\chi = \chi_c$ and $\chi = 1$.

Classical Markov's theorem [59] proves pointwise convergence of the diagonal Padé approximants $[N/N]_f$ of the function f of the type (48) with $\rho(\chi) \geq 0$ in the limit $N \to \infty$ for $\zeta \in \mathbb{C} \setminus [\mathrm{i}\chi_c, \mathrm{i}]$. Here, the diagonal Padé approximation $[N/N]_f$ of the function f means that both polynomials $P(\zeta)$ and $Q(\zeta)$ have the same order N, which is natural for the discretization (49). More general Padé approximants of the function f are $[N/M]_f$,

where N and M are the orders of the polynomials $P(\zeta)$ and $Q(\zeta)$, respectively. Theorem in [60] ensures pointwise convergence of $[N/M]_f \to f$ for $N \to \infty$ with fixed M in the disk $|\zeta| < R$ if f is the meromorphic function in that disk with exactly M poles (counted according to their multiplicity). However, the diagonal Padé approximations of the meromorphic function f generally fail to provide uniform convergence with the known counterexamples given in [61, 62]. Work [63] showed that instead the diagonal Padé approximants of meromorphic function for $N \to \infty$ have a weaker convergence in logarithmic capacity, which allows the lack of pointwise convergence along exceptional sets. Gonchar [64, 65] extended Markov's theorem on the pointwise convergence of the diagonal Padé approximants to the functions $f + r$, where f is the function of the type (48) with $\rho(\chi) > 0$ almost everywhere in $\chi \in [\chi_c, 1]$, and r is the meromorphic function away from branch cut and has no poles at branch cut. Convergence in logarithmic capacity of the diagonal Padé approximants of the analytic function $f(\zeta)$ with a finite number of branch points (this is a more general type than the type (48) because these branch points can be located away from a single line) was proven in [66–68]. That convergence occurs away from certain sets of $\mathbb{C}$ (in some cases, these sets are simple arcs). See also [69] for the recent review. All these results were obtained for Padé approximants based on the Taylor series at a single point in $\mathbb{C}$. Thus, these results do not directly apply to AGH algorithm, which is based on least squares approximation at multiple points of $\mathbb{C}$. AGH algorithm is also distinct from multipoint Padé approximation [70, 71], where the Taylor series is interpolated at multiple points in contrast to least squares in AGH algorithm. Padé approximants were also constructed based on least squares in [72] where it was conjectured that least squares-type algorithms might ensure pointwise convergence. That conjecture is consistent with our simulations.

4.3. Finding a numerical value of a location of branch point $\zeta = i\chi_c$

There are different ways to find the location of branch point $\zeta = \mathrm{i}\chi_c$ from simulations. First way is based on the decay of Fourier spectrum of $\tilde{z}(\zeta)$ for $n \gg 1$ and is described in Section 3.3. Second way is to find $\rho(\chi_n)$, $n = 1, \ldots, N$ and then determine the point $\rho(\chi_c) = 0$ by the polynomial extrapolation of $\rho(\chi_n)$. First and second ways provide comparable numerical accuracy in our simulations (typically, the relative error in χ_c is $\sim 10^{-4}$).

We found, however, that better accuracy is achieved in the third way as follows. Consider the formal series

$$\tilde{z}_{ser} = \sum_{j=0}^{\infty} \mathrm{i} e^{\mathrm{i}j\pi/4} a_j (\zeta - \mathrm{i}\chi_c)^{j/2} \tag{56}$$

in the neighborhood of the branch point $\zeta = \mathrm{i}\chi_c$. The term $ie^{\mathrm{i}j\pi/4}$ in front of the coefficients a_j is chosen for convenience to ensure that coefficients a_j take real values. The radius of convergence of that series is $2\chi_c$ as discussed in Part II [45]. Taking $M = 10 - 20$ terms in that series, one can use the nonlinear fit to determine the unknowns χ_c and a_j. Typically, we use $N_j = 30 - 40$ points $(u_n, \tilde{z}(u_n))$ such that all values u_n are inside the disk of convergence $|u_n - \mathrm{i}\chi_c| < 2\chi_c$ of the series (56). Here, values of $\tilde{z}(u_n)$ are taken from simulations of Section 3 with u_n being the numerical grid points closest to $u = 0$. The accuracy of the nonlinear fit is typically $\sim 10^{-10}$ as estimated by varying M and N_M. In Part II [45], we provide much more accurate way of calculating χ_c, which is based on the compatibility of the series (56) with Eq. (37) of Stokes wave. In contrast, the above three methods use numerical values of $(u_n, \tilde{z}(u_n))$ obtained as described in Section 3 and do not use Eq. (37) directly.

5. Stokes wave as an integral over jump at branch cut and the expansion of density ρ near a branch point

5.1. Jump at branch cut

Sokhotskii–Plemelj theorem (see, e.g. [73, 74]) applied to Eq. (48) gives

$$\tilde{z}(\mathrm{i}\chi \pm 0) = \mathrm{i}y_b + \mathrm{p.v.}\int_{\chi_c}^{1} \frac{\rho(\chi')\mathrm{d}\chi'}{\mathrm{i}(\chi - \chi')} \pm \pi\rho(\chi), \quad \chi_c < \chi < 1. \tag{57}$$

Thus, the jump of $\tilde{z}(\zeta)$ at branch cut is $-2\pi\rho(\chi)$ for crossing branch cut at $\zeta = \mathrm{i}\chi$ in counterclockwise direction.

5.2. Stokes wave as the sum of contribution from branch cuts in w complex plane

Consider a representation of Stokes wave by the density $\tilde{\rho}$ along branch cuts in complex plane w. Because of the 2π-periodicity in u direction, we write $z(w)$ as the integral over periodically located branch cuts,

$$\tilde{z}(w) = z_1 + \int_{v_c}^{\infty} \sum_{n=-\infty}^{\infty} \left(\frac{1}{w + 2\pi n - \mathrm{i}v'} - \frac{1}{b + 2\pi n - \mathrm{i}v'} \right) \tilde{\rho}(v')\mathrm{d}v', \tag{58}$$

where z_1 is the complex constant, v_c is related to χ_c by (45), a summation over n ensures the periodicity of $\tilde{z}(w)$ along u, and we replaced $\rho(\chi)$ by $\tilde{\rho}(v')$ to distinguish it from $\rho(\chi)$ in (48). Also, we introduced the additional term $-\frac{1}{b+2\pi n-\mathrm{i}v'}$, which is intended to ensure the convergence of

the integral. The constant b can be chosen at our convenience. A change of that constant results in the change of z_1.

The sum in (58) is then calculated using the identity

$$\sum_{n=-\infty}^{\infty} \frac{1}{n+a} = \pi \cot \pi a$$

giving

$$\tilde{z}(w) = z_1 + \frac{1}{2} \int_{v_c}^{\infty} \left(\cot \left[\frac{w - \mathrm{i}v'}{2} \right] - \cot \left[\frac{b - \mathrm{i}v'}{2} \right] \right) \tilde{\rho}(v') \mathrm{d}v'. \tag{59}$$

Taking the limit $Im(w) \to -\infty$, we obtain from Eqs. (59) and (48) that

$$\tilde{z}(u - \mathrm{i}\infty) = z_1 + \frac{1}{2} \int_{v_c}^{\infty} \left(\mathrm{i} - \cot \left[\frac{b - \mathrm{i}v'}{2} \right] \right) \tilde{\rho}(v') \mathrm{d}v' = \mathrm{i}y_b + \int_{\chi_c}^{1} \frac{\rho(\chi) \mathrm{d}\chi}{-\mathrm{i} - \mathrm{i}\chi}. \tag{60}$$

We set

$$\chi = \tanh \frac{v'}{2} \tag{61}$$

and

$$\rho(\chi) = \tilde{\rho}(2 \operatorname{arctanh} \chi). \tag{62}$$

We also require that $z_1 = \mathrm{i}y_b$ and then we find from Eqs. (60), (61), and (62) that

$$b = \pi. \tag{63}$$

Using the trigonometric identity

$$\cot(a - b) = \frac{1 + \tan a \tan b}{\tan a - \tan b},$$

one obtains from (59), (60), (61), (62), and (63) that

$$\tilde{z}(w) = \mathrm{i}y_b + \frac{1}{2} \int_{v_c}^{\infty} \left(\frac{\left[1 + \mathrm{i} \tan \frac{w}{2} \tanh \frac{v'}{2} \right]}{\tan \frac{w}{2} - \mathrm{i} \tanh \frac{v'}{2}} - \mathrm{i} \tanh \frac{v'}{2} \right) \tilde{\rho}(v') \mathrm{d}v'$$

$$= \mathrm{i}y_b + \frac{1}{2} \int_{v_c}^{\infty} \left(\frac{1 + \mathrm{i}\zeta\chi}{\zeta - \mathrm{i}\chi} - \mathrm{i}\chi \right) \tilde{\rho}(v') dv' = \mathrm{i}y_b + \int_{\chi_c}^{1} \frac{\rho(\chi) \mathrm{d}\chi}{\zeta - \mathrm{i}\chi}, \tag{64}$$

i.e., we recovered Eq. (48) from Eq. (58).

5.3. Expansion of $\rho(\chi)$ in powers of $\zeta - \mathrm{i}\chi_c$

Assume that we have the branch cut $(\mathrm{i}\chi_c, \mathrm{i})$ for $z(\zeta)$ in the complex plane of ζ and that the branch point at $\zeta = \mathrm{i}\chi_c$ is of square-root type. Then, we expand $\rho(\chi)$ in the following series

$$\rho(\chi) = \sum_{n=0}^{\infty} b_{2n+1}(\chi - \chi_c)^{1/2+n}. \tag{65}$$

Note that adding terms of integer powers of $(\zeta - \mathrm{i}\chi_c)$ into Eq. (65) is not allowed because it would produce logarithmic singularity at $\zeta = \mathrm{i}\chi_c$ through Eq. (48), which is incompatible with the Stokes wave as was shown in [7,13].

Integrating over χ in (48) using (65) gives

$$\begin{aligned} f(\zeta) = b_1 &\left(2\mathrm{i}\sqrt{1-\chi_c} - 2\mathrm{i}\sqrt{\chi_c + \mathrm{i}\zeta}\arctan\left[\frac{\sqrt{1-\chi_c}}{\sqrt{\chi_c+\mathrm{i}\zeta}}\right]\right) \\ &+ b_3\left(\frac{2}{3}\sqrt{1-\chi_c}(\mathrm{i} - 4\mathrm{i}\chi_c + 3\zeta) + 2\mathrm{i}(\chi_c + \mathrm{i}\zeta)^{3/2}\arctan\left[\frac{\sqrt{1-\chi_c}}{\sqrt{\chi_c+\mathrm{i}\zeta}}\right]\right) \\ &+ b_5\left(\frac{2}{15}\sqrt{1-\chi_c}\left(3\mathrm{i} - 11\mathrm{i}\chi_c + 23\mathrm{i}\chi_c^2 + 5\zeta - 35\chi_c\zeta - 15\mathrm{i}\zeta^2\right)\right. \\ &\left. - 2\mathrm{i}(\chi_c + \mathrm{i}\zeta)^{5/2}\arctan\left[\frac{\sqrt{1-\chi_c}}{\sqrt{\chi_c+\mathrm{i}\zeta}}\right]\right) + b_7(\ldots) + \ldots \end{aligned} \tag{66}$$

A series expansion of (66) at $\zeta = \mathrm{i}\chi_c$ and comparison with the series (56) result in the relations

$$b_{2j+1} = (-1)^{j+1}a_{2j+1}, \quad j = 0, 1, 2, \ldots \tag{67}$$

Note that the expansion (66) provides the relations for b_n with only odd values of n. This is because the series (65) is convergent only inside its disk of convergence, $\chi - \chi_c < r$, where r is the radius of convergence. It will be shown in Part II [45] that $r = 2\chi_c$ for $\chi_c < 1/3$. The explicit expression for $\rho(\chi)$ is unknown for $\chi_c + r < \chi < 1$, while $\rho(\chi)$ still contributes to the terms $a_{2j}(\zeta - \mathrm{i}\chi_c)^j$, $j = 0, 1, 2, \ldots$ in the series (56).

Thus, the expansion (65) together with the relations (67) provides a convenient tool to work with $\rho(\chi)$ near to $\chi = \chi_c$.

5.4. Absence of singularities in branch cut beyond the branch points $\zeta = \mathrm{i}\chi_c$ and $\zeta = \mathrm{i}$

A priori one cannot exclude the existence of singularities inside the branch cut $\zeta \in [\mathrm{i}\chi_c, \mathrm{i}]$ beyond branch points $\zeta = \mathrm{i}\chi_c$ and $\zeta = \mathrm{i}$ at its ends. Existence of such singularities was conjectured in [7, 8]. To address that

possibility, we subtracted the expansion (66) from the numerical solution of $\tilde{z}(\zeta)$ for Stokes wave. We obtained both $\tilde{z}(\zeta)$ and recovered $\rho(\chi)$ through AGH algorithm using variable precision arithmetics with ~ 200 digits to achieve a high precision in that subtraction. Typically, we used Stokes wave of the moderate nonlinearity with $\chi_c \sim 10^{-2}$ to operate with the moderate number of required Fourier harmonics. After that, the numerical values of $b_1, b_3, b_5, \ldots$ were recovered from fitting of $\rho(\chi)$ to the expansion (65) near $\chi = \chi_c$. Typically, we truncated the expansion (65) to the first three terms b_1, b_3, b_5, which results in the truncated function $f(\zeta)_{truncated}$ in the expansion (66). Also, χ_c was obtained by the procedures described in Section 4.3. Alternative way to recover b_1, b_3, b_5 is through using the expansion (41) that was also used but generally gives lower precision.

Next step was to take mth derivative of $\tilde{z}(\zeta) - f(\zeta)_{truncated}$ over ζ numerically and obtain the Padé approximation for the resulting expression $[\tilde{z}(\zeta) - f(\zeta)_{truncated}]^{(m)}$ resulting in new density $\tilde{\rho}(\chi)$. If any singularity would be present inside the branch cut, then it would correspond to singularity in $\tilde{\rho}(\chi)$. However, we did not find any sign of such singularities at least for moderate order of derivative $m = 1, 2, 3$. It suggests that $\zeta = \mathrm{i}\chi_c$ and $\zeta = \mathrm{i}$ are the only singularities in complex ζ plain. This conclusion is in agreement with the results of both [13] and Part II [45] obtained by alternative methods.

6. Conclusion

In this paper, we found numerically the Stokes solutions of the primordial Euler equations with free surface for large range of wave heights, including the approach to the limiting Stokes wave. The limiting Stokes wave emerges as the singularity reaches the fluid surface. We found from our high-precision simulations (between 32 and more than 200 digits) the Padé approximation of branch cut singularity of Stokes wave. We provided the tables of the Padé approximants for a wide range of Stokes wave steepness. These tables allow to recover Stokes wave with the minimum accuracy 10^{-26}. We show that these Padé approximants quickly converge to the jump at branch cut as the number of poles N increases with the scaling law (46), (47). We use the series expansion of the jump along branch cuts in half-integer powers to recover the square-root singularity at the branch point. We found that there are no more singularities in the finite complex plane beyond one branch point per period. Following Part II [45] is devoted to the analysis of the structure and location of branch points in infinite set of sheets of Riemann surface beyond the physical sheet of Riemann surface considered here.

Acknowledgments

The authors would like to thank Prof. S. Lau for the introduction to AGH method of Padé approximation and sharing his computer codes, which were used at the initial stage of research. The authors would like to thank the anonymous reviewer for many valuable and very helpful comments. Also, the authors thank developers of Fastest Fourier Transform in the West (FFTW) [75] and the whole GNU project [76] for developing and supporting this useful and free software. The work of S.D. and A.K. was partially supported by the National Science Foundation (Grant OCE-1131791). The work of P.L. was partially supported by the National Science Foundation (Grant DMS-1412140). The work of A.K. and P.L. on the Padé approximation was supported by Russian Science Foundation (Grant 14-22-00259).

Appendix A: Derivation of dynamical equations

In this Appendix, we adapt the work of [42] to the case of the periodic boundary conditions deriving the basic dynamical equations (11) and (12) for 2D ideal hydrodynamics with free surface in conformal variables. We use similar notations to [42] and provide steps of the derivation skipped in [42].

A.1. Hamiltonian after conformal map

It was shown in [77], that the potential flow of an ideal fluid with free surface is the canonical Hamiltonian system with canonical variables η (5) and ψ (6). Canonical Hamiltonian equations

$$\frac{\partial \eta}{\partial t} = \frac{\delta H}{\delta \psi}, \quad \frac{\partial \psi}{\partial t} = -\frac{\delta H}{\delta \eta} \tag{A.1}$$

are equivalent to the boundary conditions (3) and (4). Here, H is the Hamiltonian (please note that in this Appendix, the symbol H stands for the Hamiltonian, while in all other sections H is the wave height) that coincides with the total energy (the sum of the kinetic energy T and the potential energy U) per spatial period of wave λ,

$$H = T + U = \frac{1}{2}\int_{-\lambda/2}^{\lambda/2} \mathrm{d}x \int_{-\infty}^{\eta} (\nabla\Phi)^2 \mathrm{d}y + \frac{g}{2}\int_{-\lambda/2}^{\lambda/2} \eta^2 \mathrm{d}x,$$

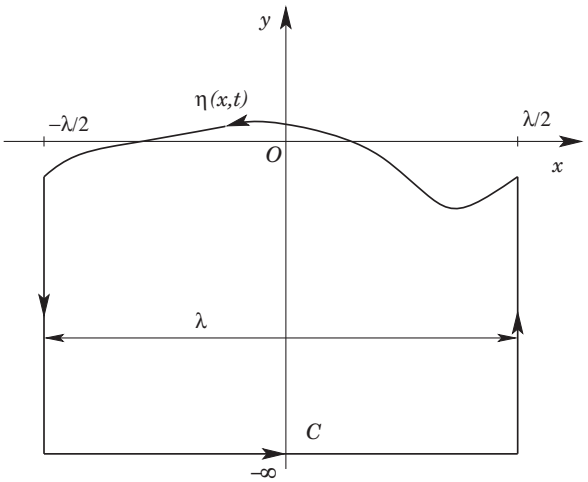

Figure A1. A schematic of one period of a wave with a counterclockwise contour of integration for application of Green's theorem.

and without loss of generality the fluid density is set to one. One has to express the kinetic energy

$$T = \frac{1}{2}\int_{-\lambda/2}^{\lambda/2} \mathrm{d}x \int_{-\infty}^{\eta} (\nabla\Phi)^2 \mathrm{d}y \tag{A.2}$$

through the canonical variables η and ψ, which generally requires to solve the Laplace equation (2) with the boundary conditions (3), (4), and (6) and $\Phi(x, y, t)|_{y\to-\infty} = 0$ in the region $-\frac{\lambda}{2} \le x < \frac{\lambda}{2}$, $-\infty < y \le \eta(x, t)$. That region is schematically shown in Fig. A1. Using relations

$$\nabla\cdot(\Phi\nabla\Phi) = (\nabla\Phi)^2 + \Phi\nabla^2\Phi, \quad (\nabla\Phi)^2 = \frac{\partial}{\partial x}\left(\Phi\frac{\partial\Phi}{\partial x}\right) + \frac{\partial}{\partial y}\left(\Phi\frac{\partial\Phi}{\partial y}\right),$$

which are valid for the harmonic function Φ (2), and applying Green's theorem to Eq. (A.2) one obtains that

$$\begin{aligned} 2T &= \int_{-\lambda/2}^{\lambda/2}\int_{-\infty}^{\eta} \left\{\frac{\partial}{\partial x}\left(\Phi\frac{\partial\Phi}{\partial x}\right) + \frac{\partial}{\partial y}\left(\Phi\frac{\partial\Phi}{\partial y}\right)\right\}\mathrm{d}x\mathrm{d}y \\ &= \int_{C}\left(-\Phi\frac{\partial\Phi}{\partial y}\mathrm{d}x + \Phi\frac{\partial\Phi}{\partial x}\mathrm{d}y\right). \end{aligned} \tag{A.3}$$

Here, C is a positively (counterclockwise) oriented contour along the boundary of the periodic domain occupied by fluid shown in Fig. A1.

A sum of integrals along left-hand side (l.h.s.) and right-hand side (r.h.s.) (vertical segments) of the contour vanishes due to periodicity. Integral along lower part of the contour (horizontal segment) is zero due to the boundary condition on potential $\Phi_{y=-\infty} = 0$. Notice that in the case of finite depth fluid with a rigid flat bottom $y = -h$, the integral along similar lower segment $y = -h$ is also zero because the boundary condition at the finite depth bottom is $\Phi_y|_{y=-h} = 0$ (zero vertical velocity at the bottom) and $\mathrm{d}y = 0$. Then, Eq. (A.3) is reduced to the following line integral

$$2T = \int\limits_{x=\lambda/2,\ y=\eta(x,t)}^{x=-\lambda/2} \left(-\Phi\frac{\partial\Phi}{\partial y}\mathrm{d}x + \Phi\frac{\partial\Phi}{\partial x}\mathrm{d}y\right). \tag{A.4}$$

We use the time-dependent conformal transformation (7) and (8) to relate partial derivatives in x, y and u, v as follows:

$$\frac{\partial\Phi}{\partial u} = \frac{\partial\Phi}{\partial x}x_u + \frac{\partial\Phi}{\partial y}y_u,$$
$$\frac{\partial\Phi}{\partial v} = \frac{\partial\Phi}{\partial x}x_v + \frac{\partial\Phi}{\partial y}y_v,$$

which implies that

$$\frac{\partial\Phi}{\partial x} = \frac{\Phi_u x_u - \Phi_v y_u}{x_u^2 + y_u^2}, \tag{A.5}$$

$$\frac{\partial\Phi}{\partial y} = \frac{\Phi_u y_u + \Phi_v x_u}{x_u^2 + y_u^2}, \tag{A.6}$$

where we also used Cauchy–Riemann equations $x_u = y_v$ and $x_v = -y_u$ for the conformal map $z(w)$. Here and in subsequent equations, the subscripts mean partial derivatives, e.g., $x_t = \frac{\partial}{\partial t}x, x_u = \frac{\partial}{\partial u}x$, etc.

Substituting (A.5) and (A.6) into (A.4), using relations $\mathrm{d}x = x_u\mathrm{d}u$ and $\mathrm{d}y = y_u\mathrm{d}u$ on the line $w = u$ one obtains that

$$2T = \int\limits_{\lambda/2}^{-\lambda/2} (-\Phi_v\Phi)|_{v=0}\,\mathrm{d}u = \int\limits_{-\lambda/2}^{\lambda/2} \Phi_v\Phi|_{v=0}\,\mathrm{d}u. \tag{A.7}$$

Here, we took into account the orientation of the contour and conditions (8) on conformal transformation.

Sokhotskii–Plemelj theorem (57) (see, e.g. [73, 74]) allows to express a real part of the function, which is analytic in the lower (upper) half-plane through the imaginary part (and vice versa) at the real line $u = w$ using the Hilbert transformation (14). For a conformal transformation

$z(w,t) = x(w,t) + \mathrm{i}y(w,t)$, such relations are given by (31). A complex velocity potential $\Pi(z,t) = \Phi + \mathrm{i}\Theta$ is the analytic function in the fluid domain $-\infty < y \le \eta(x,t)$, where Θ is the stream function. The conformal transformation $z = z(w,t)$ (7) ensures that Π remains analytic function after transforming from z to w variable with the lower half-plane $\mathbb{C}^-$ being the domain of analyticity in w. Similar to Eq. (31), real and imaginary parts of Π are related at the real line $u = w$ through the Hilbert transformation as follows:

$$\Theta = \hat{H}\Phi, \quad \Phi = -\hat{H}\Theta, \tag{A.8}$$

where we assumed the decaying boundary condition $\Phi|_{v=-\infty} = \Theta|_{v=-\infty} = 0$. Here, we abuse notation and use the same Π and Φ both for independent variables w and z : $\tilde{\Phi}(w,t) \equiv \Phi(z,t)$ and $\tilde{\Pi}(w,t) \equiv \Pi(z,t)$, i.e., we omit tilde.

Also the analyticity of Π implies that the velocity potential Φ is the harmonic function satisfying the Laplace equation (2) both in x, y variables and similarly

$$\nabla^2 \Phi(u,v,t) = 0$$

in variables u and v. Using Cauchy–Riemann equations (17) and the relations (A.8), one obtains that

$$\Phi_v = -\hat{H}\Phi_u. \tag{A.9}$$

Substituting (A.9) into (A.7), we express the kinetic energy in terms of canonical variable ψ as follows:

$$2T = \int_{-\lambda/2}^{\lambda/2} \Phi_v \Phi|_{v=0}\, \mathrm{d}u = -\int_{-\lambda/2}^{\lambda/2} \psi \hat{H}\psi_u \mathrm{d}u. \tag{A.10}$$

Here, we used the definition (6) which in w plane turns into $\psi(u,t) \equiv \Phi(u, v=0, t)$ as follows from the mapping of the fluid surface into the real line $v = 0$. Then, the Hamiltonian in terms of variables on the surface takes the following form

$$H = -\frac{1}{2}\int_{-\lambda/2}^{\lambda/2} \psi \hat{H}\psi_u \mathrm{d}u + \frac{g}{2}\int_{-\lambda/2}^{\lambda/2} y^2 x_u \mathrm{d}u. \tag{A.11}$$

A.2. Least action principle in conformal variables

We use the constrained Lagrangian formulation to obtain the dynamical equations in conformal variables at fluid surface. A time dependence of the map (7) implies that we have to ensure the analyticity of that map through

the appropriate constraint. We discuss the Lagrangian dynamics first and add the corresponding constraint later in this section. Equations (A.1) realize extremum of an action

$$S = \int_{t_1}^{t_2} L\,\mathrm{d}t, \tag{A.12}$$

with the Lagrangian

$$L = \int_{-\lambda/2}^{\lambda/2} \psi \frac{\partial \eta}{\partial t}\mathrm{d}x - H. \tag{A.13}$$

The first term here has to be converted from the integral over x into u variable. Consider mapping $(x,t) \to (u,\tau)$, which is the change of parameterization of the surface under the conformal map. Here, $\tau = t$. Transformation $u = u(x,t)$ is the inverse to the conformal map $x = x(u,\tau)$. The fluid surface $\eta(x,t)$ after transformation corresponds to $y(u,\tau)$. We express $\partial\eta/\partial t$ by the chain rule as follows:

$$\frac{\partial \eta}{\partial t} = \frac{\partial y}{\partial \tau}\frac{\partial \tau}{\partial t} + \frac{\partial y}{\partial u}\frac{\partial u}{\partial t} = \frac{\partial y}{\partial \tau} + \frac{\partial y}{\partial u}\frac{\partial u}{\partial t}. \tag{A.14}$$

To find $\partial u/\partial t$, here we express full differentials of x and t through u and τ as follows:

$$\begin{pmatrix} \mathrm{d}x \\ \mathrm{d}t \end{pmatrix} = \begin{pmatrix} x_u & x_\tau \\ t_u & t_\tau \end{pmatrix} \begin{pmatrix} \mathrm{d}u \\ \mathrm{d}\tau \end{pmatrix} \equiv J \begin{pmatrix} \mathrm{d}u \\ \mathrm{d}\tau \end{pmatrix}. \tag{A.15}$$

Taking into account that $\tau = t$, one obtains the Jacobian matrix

$$J = \begin{pmatrix} x_u & x_\tau \\ 0 & 1 \end{pmatrix}. \tag{A.16}$$

Inverse procedure for full differentials of u and τ through x and t yields that

$$\begin{pmatrix} \mathrm{d}u \\ \mathrm{d}\tau \end{pmatrix} = \begin{pmatrix} \partial u/\partial x & \partial u/\partial t \\ \partial \tau/\partial x & \partial \tau/\partial t \end{pmatrix} \begin{pmatrix} \mathrm{d}x \\ \mathrm{d}t \end{pmatrix} = J^{-1} \begin{pmatrix} \mathrm{d}x \\ \mathrm{d}t \end{pmatrix}. \tag{A.17}$$

Comparing entries of the matrix in (A.17) with inverse of (A.16), one gets

$$\frac{\partial u}{\partial t} = -\frac{x_\tau}{x_u}. \tag{A.18}$$

Substituting (A.18) into (A.14) yields

$$\frac{\partial \eta}{\partial t} = y_\tau - y_u \frac{x_\tau}{x_u}. \tag{A.19}$$

We use the Lagrangian (A.13) to substitute it into the action (A.12). Consider the first term in the action,

$$S = \int\int L\mathrm{d}t = \int\int \psi \frac{\partial \eta}{\partial t}\mathrm{d}x\mathrm{d}t + \ldots \tag{A.20}$$

and perform a change of variables in the integral as $\mathrm{d}x\mathrm{d}t = \det(J)\mathrm{d}u\mathrm{d}\tau = x_u\mathrm{d}u\mathrm{d}\tau$. Together with the expression (A.19), it results in

$$\begin{aligned}\int\int \psi \frac{\partial \eta}{\partial t}\mathrm{d}x\mathrm{d}t &= \int\int \psi \left(y_\tau - y_u \frac{x_\tau}{x_u}\right) x_u \mathrm{d}u\mathrm{d}\tau \\ &= \int\int \psi(y_\tau x_u - y_u x_\tau)\mathrm{d}u\mathrm{d}\tau. \end{aligned} \tag{A.21}$$

Using (A.11), (A.13), and (A.21) and adding the analyticity constraint (31) ensuring that $y - y_0 = \hat{H}\tilde{x}$ and taking into account that $\tau = t$ as well, we obtain a new constrained Lagrangian

$$\begin{aligned} L = \int_{-\lambda/2}^{\lambda/2} \psi(y_t x_u - y_u x_t)\mathrm{d}u + \frac{1}{2}\int_{-\lambda/2}^{\lambda/2} \psi \hat{H}\psi_u \mathrm{d}u - \frac{g}{2}\int_{-\lambda/2}^{\lambda/2} y^2 x_u \mathrm{d}u \\ + \int_{-\lambda/2}^{\lambda/2} (y - y_0 - \hat{H}\tilde{x}) f \mathrm{d}u, \end{aligned} \tag{A.22}$$

where f is the Lagrange multiplier for the analyticity constraint.

A.3. Variations of action

We now obtain the dynamical equations from the Hamilton least action principle. Vanishing of variational derivative $\delta S/\delta\psi = 0$ of the action (A.12) with the Lagrangian (A.22) over potential ψ on the surface yields the following expression

$$y_t x_u - y_u x_t + \hat{H}\psi_u = 0. \tag{A.23}$$

This equation is nothing else but kinematic boundary condition (3) after the conformal map into w plane.

Two conditions $\delta S/\delta x = 0$ and $\delta S/\delta y = 0$ result in equations

$$y_u \psi_t - y_t \psi_u + g y y_u = \hat{H} f, \tag{A.24}$$

$$-x_u \psi_t + x_t \psi_u - g y x_u = f, \tag{A.25}$$

which are turned into a single equation by excluding the Lagrange multiplier f giving

$$y_u\psi_t - y_t\psi_u + \hat{H}(x_u\psi_t - x_t\psi_u) + g[yy_u + \hat{H}(yx_u)] = 0. \tag{A.26}$$

Equations (A.23) and (A.26) recover the implicit dynamical equations (11) and (12).

A.4. Zeroth harmonic in implicit dynamical equations (11) and (12) and conservation of momentum

Consider Fourier transformations of the surface elevation $y(u,t)$ and the velocity potential on surface ψ with respect to conformal coordinate u,

$$\begin{aligned} y(u,t) &= y_0(t) + \sum_{k\neq 0} y_k(t)\mathrm{e}^{\mathrm{i}ku}, \\ \psi(u,t) &= \psi_0(t) + \sum_{k\neq 0} \psi_k(t)\mathrm{e}^{\mathrm{i}ku}. \end{aligned} \tag{A.27}$$

Here, zeroth harmonics $y_0(t)$ and $\psi_0(t)$ are written separately and are given by

$$y_0(t) = \frac{1}{\lambda}\int_{-\lambda/2}^{\lambda/2} y(u,t)\mathrm{d}u, \quad \psi_0(t) = \frac{1}{\lambda}\int_{-\lambda/2}^{\lambda/2} \psi(u,t)\mathrm{d}u. \tag{A.28}$$

Both y_0 and ψ_0 must be time-independent to ensure that the fluid is at rest for $v \to -\infty$ (in the depth of the fluid) and satisfies the dynamic boundary condition (4).

One can rewrite Eq. (A.26) in the following form

$$y_u\psi_t - y_t\psi_u = -\hat{H}(x_u\psi_t - x_t\psi_u + yx_u) - \frac{g}{2}\frac{\partial}{\partial u}y^2. \tag{A.29}$$

A zeroth Fourier harmonic of the r.h.s. of Eq. (A.29) vanishes because the term in parenthesis is multiplied by $\hat{H}$, which removes any zeroth harmonic, and the remaining term is the partial derivative over u. Respectively, the zeroth harmonic of the l.h.s. of Eq. (A.29) must vanish. Integrating that l.h.s. to obtain the zeroth harmonic, using Eq. (A.29) and integrating by parts over u one obtains that

$$\frac{1}{\lambda}\int_{-\lambda/2}^{\lambda/2}(y_u\psi_t - y_t\psi_u)\mathrm{d}u = \frac{1}{\lambda}\int_{-\lambda/2}^{\lambda/2}(y_u\psi_t + y_{ut}\psi)\mathrm{d}u = \frac{1}{\lambda}\frac{\partial}{\partial t}\int_{-\lambda/2}^{\lambda/2}\psi y_u\mathrm{d}u = 0, \tag{A.30}$$

where we used a periodicity of ψ and y in u. Thus, $\int_{-\lambda/2}^{\lambda/2}\psi y_u\mathrm{d}u$ is the integral of motion. To find a physical meaning of that integral, we note that natural candidates for conserved quantities are the components of the total

momentum of fluid along x and y directions. Taking into account that fluid density is one, we obtain x component of momentum P_x as an integral of the horizontal velocity inside fluid, which gives

$$P_x = \int_{-\lambda/2}^{\lambda/2} \mathrm{d}x \int_{-\infty}^{\eta(x,t)} \Phi_x \mathrm{d}y = \int_C \Phi \mathrm{d}y = \int_{\lambda/2}^{-\lambda/2} \Phi \left.\frac{\partial y}{\partial x}\right|_{y=\eta(x,t)} \mathrm{d}x = -\int_{-\lambda/2}^{\lambda/2} \psi y_u \mathrm{d}u. \quad \text{(A.31)}$$

Here, we applied Green's theorem to positively oriented contour C shown in Fig. A1. Due to periodicity of functions and decaying boundary condition $\Phi(x, y, t)|_{y\to-\infty} = 0$, only integral along the surface is nonzero. Comparison of Eqs. (A.30) and (A.31) shows that consistency of Eq. (A.29) is ensured by the conservation of the horizontal component P_x of the total momentum of the fluid.

Applying the Hilbert transformation $\hat{H}$ to Eq. (A.29) and using the identity (30), one obtains that

$$x_u\psi_t - x_t\psi_u + yx_u - q_0 = \hat{H}\left(y_u\psi_t - y_t\psi_u + \frac{g}{2}\frac{\partial}{\partial u}y^2\right), \quad \text{(A.32)}$$

where q_0 is the zeroth Fourier harmonic of $x_u\psi_t - x_t\psi_u + yx_u$. To find q_0, we proceed similar to Eqs. (A.30) and (A.31) to find that

$$q_0 = \frac{1}{\lambda}\int_{-\lambda/2}^{\lambda/2}(x_u\psi_t - x_t\psi_u + yx_u)\mathrm{d}u = \frac{1}{\lambda}\frac{\partial}{\partial t}\int_{-\lambda/2}^{\lambda/2}\psi x_u \mathrm{d}u + \frac{1}{\lambda}\int_{-\lambda/2}^{\lambda/2} yx_u \mathrm{d}u, \quad \text{(A.33)}$$

where $\int_{-\lambda/2}^{\lambda/2}\psi x_u \mathrm{d}u$ is the integral of motion corresponding to the conservation of the vertical component P_y of the total momentum of fluid,

$$P_y = \int_{-\lambda/2}^{\lambda/2} \mathrm{d}x \int_{-\infty}^{\eta(x,t)} \Phi_y \mathrm{d}y = \int_C -\Phi \mathrm{d}x = \int_{-\lambda/2}^{\lambda/2} \psi x_u \mathrm{d}u. \quad \text{(A.34)}$$

Then, Eqs. (A.33) and (A.34) imply that q_0 is the integral of motion given by

$$q_0 = \frac{1}{\lambda}\int_{-\lambda/2}^{\lambda/2} yx_u \mathrm{d}u = \frac{1}{\lambda}\int_{-\lambda/2}^{\lambda/2} \eta(x,t)\mathrm{d}x \quad \text{(A.35)}$$

and representing a conservation of the total mass of fluid. Also according to Eq. (19), we set $q_0 = 0$ in this paper.

Appendix B: Alpert–Greengard–Hagstrom algorithm and Stokes wave

In this Appendix, we describe an efficient algorithm for Padé approximation of the function on a discrete grid, following original work [38] and work by [39] where more detailed explanation and further development of the algorithm were presented.

Consider 2π-periodic complex-valued function $f(u) = z(u) - u - \mathrm{i}y_b$ defined on a grid with nodes $u_j \in [-\pi, \pi]$. Values of the function at the grid points are denoted as $f_j = f(u_j)$. We look for an approximation of $f(u)$ in the form of a ratio of two polynomials $P(u)$ and $Q(u)$, i.e., the Padé approximation. We briefly describe AGH algorithm in a general way with additional comments for our particular case. As it was mentioned in Section 4, we use the second conformal map $\zeta = \tan(u/2)$. The introduction of auxiliary variable ζ allows to consider the real line $\zeta \in \mathbb{R}$ as opposed to considering a finite interval $u \in [-\pi, \pi]$, while the infinity along the imaginary axis is mapped into imaginary unit i and 2π-periodicity in u direction is ensured. Without loss of generality, we assume that $f(\pm\pi) = 0$. In this paper, we take $f(u) = z(u) - u - \mathrm{i}y_b = \tilde{z}(u) - \mathrm{i}y_b$ (see Eqs. (48) and (49) for comparison). Condition $f(\pm\pi) = 0$ allows to consider P and Q such that the degree of polynomials is $\deg Q = 1 + \deg P = N$, where the integer N is allowed to vary. We are looking for the convergence of the rational approximation to f,

$$\frac{P(\zeta)}{Q(\zeta)} \to f(\zeta),$$

in a sense of solving a minimization problem

$$\min_{P,Q} \int_{-\pi}^{+\pi} \left| \frac{P(u)}{Q(u)} - f(u) \right|^2 \mathrm{d}u. \tag{B.1}$$

That minimization problem is challenging because Q in the denominator makes (B.1) nonlinear problem. In the transformed variable ζ, the problem (B.1) remains nonlinear and is reduced to

$$\min_{P,Q} \int_{-\infty}^{+\infty} \left| \frac{P(\zeta)}{Q(\zeta)} - f(\zeta) \right|^2 \frac{\mathrm{d}\zeta}{\zeta^2 + 1}. \tag{B.2}$$

In AGH algorithm, the complexity of nonlinearity is bypassed by solving instead of (B.1), a sequence of linear least-square problems

$$\min_{P^{(i+1)}, Q^{(i+1)}} \int_{-\infty}^{+\infty} \left| \frac{P^{(i+1)}(u)}{Q^{(i)}(u)} - \frac{Q^{(i+1)}(u)}{Q^{(i)}(u)} f(u) \right|^2 \mathrm{d}u, \ i = 1, 2, \ldots \tag{B.3}$$

We define an inner product

$$\langle f, g\rangle_i = \int_{-\infty}^{+\infty} f(u)\bar{g}(u)w_i(u)\mathrm{d}u, \tag{B.4}$$

with a weight function $w_i(u) = \frac{1}{|Q^{(i)}(u)|^2}$ (for ζ-plane, the formula for the weight is modified to be $w_i(\zeta) = 1/(|Q^{(i)}(\zeta)|^2(\zeta^2+1))$). Then, the previous least squares problem can be rewritten as follows:

$$\min_{P^{(i+1)}, Q^{(i+1)}} || - P^{(i+1)}(u) + Q^{(i+1)}(u)f(u)||_i, \tag{B.5}$$

where

$$||g(u)||_i^2 = \langle g, g\rangle_i$$

is the norm.

As it was shown in [38], the solution of the least squares problem (B.5) is equivalent to the solution of

$$\langle -P^{i+1} + Q^{i+1}f(u), h_n(u)\rangle_i = 0,$$

for $n = 1, \ldots, 2N$, with $h_n(u)$ defined as follows

$$\begin{cases} u^{n/2-1}, & \text{for} \quad n = 2, 4, 6, \ldots, 2N, \\ u^{(n-1)/2}f(u), & \text{for} \quad n = 1, 3, 5, \ldots, 2N-1, \end{cases} \tag{B.6}$$

which are nothing else but

$$f(u), 1, uf(u), u, u^2f(u), \ldots, u^{N-1}f(u), u^{N-1}, u^Nf(u).$$

This claim can be proven by variation of mth coefficient of $P(u)$ (for even $n = 2m+2$) and $Q(u)$ (for odd $n = 2m+1$). We put coefficient at the leading power of $Q(u)$ to be equal to one. Thus, we need to find $2N$ coefficients for two polynomials.

We orthogonalize $2N+1$ functions $h_n(u)$ using Gramm–Schmidt orthogonalization procedure,

$$g_n(u) = \begin{cases} f(u), & \text{for} \quad n = 1, \\ 1 - c_{21}f(u), & \text{for} \quad n = 2, \\ ug_{n-2}(u) - \sum_{j=1}^{\min\{4,n-1\}} c_{nj}g_{n-j}(u), & \text{for} \quad n = 3, \ldots, 2N+1, \end{cases} \tag{B.7}$$

where real constants c_{nj} are given by

$$c_{nj} = \begin{cases} \dfrac{\langle 1, f(u)\rangle_i}{\langle f(u), f(u)\rangle_i}, & \text{for} \quad n = 2 \quad \text{and} \quad j = 1, \\ \dfrac{\langle (ug_{n-2}, g_{n-j}\rangle_i}{\langle g_{n-j}, g_{n-j}\rangle_i}, & \text{for} \quad n = 3, \ldots, 2N+1 \text{ and } \quad j = 1, \ldots, \min\{4, n-1\}. \end{cases} \tag{B.8}$$

Then, we obtain that

$$g_{2N+1} = -P^{(i+1)} + f(u)Q^{(i+1)}, \tag{B.9}$$

because $P^{(i+1)}$ and $Q^{(i+1)}$ are computed from recurrence coefficients c_{nj} by splitting into even- and odd-numbered parts.

For our purposes of finding the jump at branch cut, it is convenient to represent a ratio of $P(u)$ and $Q(u)$ as a partial fraction decomposition which results in a sum of simple poles,

$$\frac{P(u)}{Q(u)} = \sum_{n=1}^{N} \frac{\gamma_n}{u - \chi_n}. \tag{B.10}$$

To compute r.h.s. of Eq. (B.10), we find zeros χ_n, $n = 1, 2, \ldots, N$ of $Q(u)$ using Newton's iterations. At the first step, equation $Q(u) = 0$ is solved by Newton's iterations, which gives the first zero $u = \chi_1$. At the second step, we consider the modified function $\tilde{Q}_1 \equiv Q/(u - \chi_1)$ and use Newton's iterations to find χ_2 from $\tilde{Q}_1 = 0$. At the third step, we define $\tilde{Q}_2 \equiv \tilde{Q}_1/(u - \chi_2)$ and use Newton's iterations to find χ_3 from $\tilde{Q}_2 = 0$. We proceed in a similar way with $\tilde{Q}_n \equiv \tilde{Q}_{n-1}/(u - \chi_n)$, $n = 3, \ldots, N-1$ until all N zeros of Q are found. Then, the coefficients γ_n are given by the following standard expression

$$\gamma_n = \frac{P(\chi_n)}{Q'(\chi_n)} \tag{B.11}$$

for the partial fraction decomposition. Here, the derivative $Q'(u)$ is obtained as follows. We exclude $f(u)$ from Eq. (B.9) using the recurrence relations (B.7). After that, we differentiate the resulting expression and solve it for $Q'(u)$.

Appendix C: Tables of Stokes waves

Using the Padé approximation, introduced in Section 4, one can approximate Stokes wave for each value of the scaled height H/λ as a sum of

poles

$$z(w) \simeq z_{pade}(u) \equiv w + \mathrm{i}y_b + \sum_{n=1}^{N} \frac{\gamma_n}{\tan(w/2) - \mathrm{i}\chi_n}. \tag{C.1}$$

Here, N is the number of poles in the Padé approximation. Using AGH algorithm (see Appendix B), we found that all poles for all values of H/λ are located on the imaginary axis.

We provide Tables 1-C for four particular cases of Stokes waves with wave heights ranging from $H/L \simeq 0.031791$ to $H/L \simeq 0.141058$. Complete library of computed waves can be accessed through the web link [78] as well as through the electronic attachments to Ref. [79]. These data of Padé approximation allow to recover the Stokes wave with the relative accuracy of at least 10^{-26} (for the vast majority of cases, the actual accuracy is higher by several orders of magnitude). First and second columns of both Tables and electronic files in Refs. [78, 79] represent values of χ_n and γ_n, respectively. Additionally, a third column in electronic files provides the values of $\rho_{n,N}$, $n = 1, 2, \ldots, N$ calculated from data of the first two columns using Eqs. (51a), (54), and (55).

We used three quantities to characterize the accuracy of our numerical Stokes wave solution and its Padé approximation. First quantity is the residue

$$R(y) \equiv N^{-1/2} \left(\sum_{j=1}^{M} |\hat{L}_0 y(u_j)|^2 \right)^{1/2}$$

of Eq. (37). $R(y)$ characterizes the convergence of our iteration algorithm described in Section 3.1 to the Stokes wave. Here, $M = 2k_{max}$ is the number of grid points u_j used in the discretization of $z(u)$. Second quantity is the relative error of Padé approximation

$$err_{pade} = \left(\frac{\sum_{j=1}^{M} |z(u_j) - z_{pade}(u_j)|^2}{\sum_{j=1}^{M} |z(u_j)|^2} \right)^{1/2}$$

of our numerical solution $z(u_j)$. Third quantity is the amplitude of the highest Fourier harmonics $|\hat{z}_{k_{max}}|$ used in FFT.

We balanced these three quantities in our simulation to achieve the most efficient and reliable approximants of Stokes waves. Typically, we chose k_{max} large enough such that $|\hat{z}_{k_{max}}| < M^{-1/2} 10^{-26}$ to ensure that our discretization error is below 10^{-26}. Here, the factor $M^{-1/2}$ characterizes the accumulation of round-off error in FFTs. A convergence of numerical iterations down to

Table C1

Data for Padé Approximation of the Wave with Velocity $c = 1.005$, the Steepness $H/\lambda = 0.031791185830078550217424174610939$, and $y_b = -0.094819818875344225940453182945545$. Parameters of Simulations and Padé Approximation are $M = 16384$, $R(y) \simeq 3.64 \times 10^{-33}$, $err_{pade} \simeq 4.65 \times 10^{-31}$, and the Smallest Fourier Harmonic had Value $|\hat{z}_{k_{max}}| \simeq 1.00 \times 10^{-39}$

k	χ_k	γ_k
1	9.960410926063350838629927461086 61e-01	7.869552677988157798969409753847 30e-03
2	9.789729250875445172888517550054 98e-01	1.589382086499895499702201560075 58e-02
3	9.495696039189825344346113276595 88e-01	2.092704779146660674627624449578 13e-02
4	9.104061186787678010118840229983 71e-01	2.307728553092327749219270329785 93e-02
5	8.646947688440237758493182926327 06e-01	2.278218233955356162992824674540 14e-02
6	8.157843926449677882643709022390 31e-01	2.067815693342508983225820736170 42e-02
7	7.667745188044647471112111332869 36e-01	1.745050182918683906672019765498 62e-02
8	7.202839012067852205952814179790 68e-01	1.371915186205552703870528555878 68e-02
9	6.783654204131271307510571417053 42e-01	9.979034893934588248110470184706 10e-03
10	6.425274847908419676615854772314 96e-01	6.587399446001104384033942670242 05e-03
11	6.138146677650695620129857020142 92e-01	3.780226209360030420363906187924 91e-03
12	5.929083157742315710201020784180 28e-01	1.700684389166557586805616649692 51e-03
13	5.802208826392953721044026130453 57e-01	4.279395361919985118980051772408 95e-04

Table C2

Data for Padé Approximation of the Wave with Velocity $c = 1.051$, the Steepness $H/\lambda = 0.10042675172528485854673515635249$, and $y_b = -0.25732914098527682158156915646871$. Parameters of Simulations and Padé Approximation are $M = 16384$, $R(y) \simeq 5.19 \times 10^{-32}$, $err_{pade} \simeq 1.69 \times 10^{-31}$, and the Smallest Fourier Harmonic had Value $|\hat{z}_{k_{max}}| \simeq 1.00 \times 10^{-37}$

k	χ_k	γ_k
1	9.95104877443162988543285604210300e-01	9.86344259137750131929660816853428e-03
2	9.74036453796113160099814623502153e-01	2.04507668432927246329100238980833e-02
3	9.37570348097817646693771937993553e-01	2.79392155141519735983551710052556e-02
4	8.88478375680990825839360752138 62e-01	3.23466950514503536891484865775305e-02
5	8.30226745019764721513358604279726e-01	3.40147781594254640293216855633111e-02
6	7.66333992991599455804305516283483e-01	3.35031653839781443242921103012960e-02
7	7.00044654389407424698796692053902e-01	3.14489535896823273634285653396772e-02
8	6.34030062620564487061621925382604e-01	2.84500818501058994363745193170182e-02
9	5.70306175038391450182479612388228e-01	2.49972283728050063777939045774063e-02
10	5.10259067527902434999804572718914e-01	2.14511658748252720344184761694938e-02
11	4.54736803912594713785686635920502e-01	1.80506679368664453110659093724408e-02

(*Continued*)

Table C2
Continued

k	χ_k	γ_k
12	4.04166063099136862080187337641328e-01	1.49353242488736140402002871952586e-02
13	3.58666569676145947416712220270910e-01	1.21719831322217078183473222652247e-02
14	3.18149576080072883402812844826148e-01	9.77859794087821305028150640251530e-03
15	2.82395821449537219671027831006306e-01	7.74304960914297497673324174361282e-03
16	2.51113624911206124013006119628666e-01	6.03673166180751660604462350895498e-03
17	2.23980136883660703565243361779229e-01	4.62368871094252860720889700284368e-03
18	2.00669410169964201214033391681290e-01	3.46637996984113299044046402602488e-03
19	1.80870715726851513117763940777923e-01	2.52906751261377992038440816275726e-03
20	1.64299946133899344356900387886524e-01	1.77962987225519971005973434397249e-03
21	1.50706307186061197360270221491920e-01	1.19038860012342014795358493343618e-03
22	1.39875923302152112463866847539994e-01	7.38354660230910637368329193600582e-04
23	1.31633517886184493678824771993353e-01	4.05164363997062298811235878087573e-04
24	1.25842975665215746611096122396649e-01	1.76877312168739070195683856144061e-04
25	1.22407333541749966033626434463374e-01	4.37430353029634816661994533800963e-05

Table C3

Data for Padé Approximation of the Wave with Velocity $c = 1.0929$, the Steepness $H/\lambda = 0.13825830866311310404416736817381$, and $y_b = -0.29153391724312882929999650320 09$. Parameters of Simulations and Padé Approximation are $M = 65536$, $R(y) \simeq 2.59 \times 10^{-31}$, $err_{pade} \simeq 1.01 \times 10^{-32}$, and the Smallest Fourier Harmonic had Value $|\hat{z}_{k_{max}}| \simeq 5.00 \times 10^{-38}$

k	χ_k	γ_k
1	9.954338259326085501323840348572 13e-01	9.065139686595942639941549838590 22e-03
2	9.757207327298723616616390754455 56e-01	1.881041724798676256079883776650 13e-02
3	9.414585806990367969983989749500 63e-01	2.580242682400627707377745051110 02e-02
4	8.950720791981099348658101255969 55e-01	3.007603153027648717903697068337 79e-02
5	8.396033688600360062788108209839 49e-01	3.191678517911005432446988074890 31e-02
6	7.782467078461258645302697380953 48e-01	3.179007767615355293105958799648 77e-02
7	7.139774635954800039119191533274 80e-01	3.023354673070953858782308779159 97e-02
8	6.493143751272693580257907239638 70e-01	2.776253841587461060851492287734 01e-02
9	5.862154659289895769511203662455 81e-01	2.481078428845997070485208159112 64e-02
10	5.260779374477518729842757281015 22e-01	2.170683511443522377601783718530 73e-02
11	4.698024074039504859655040299969 14e-01	1.867629415251176997453766702895 00e-02
12	4.178862693761100400458688195922 73e-01	1.585799691440043491249612582542 60e-02
13	3.705214441823407638844200276668 27e-01	1.332485107367400595858129921622 63e-02
14	3.276824397559602135104673636060 42e-01	1.110372838809772327817086869350 09e-02
15	2.891987225491722396077215843436 98e-01	9.191852851050633186230966178611 30e-03
16	2.548104663546661958166653706869 97e-01	7.569078251493162246283659744106 75e-03

(*Continued*)

Table C3
Continued

k	χ_k	γ_k
17	2.24209367334721589574533037466343e-01	6.20644453419544059242384682030945e-03
18	1.97067225067065397541246930106441e-01	5.07177162315234989673990118919696e-03
19	1.73055091362268451120364081334665e-01	4.13307962854491967554778057762908e-03
20	1.51855462026532436104149361379210e-01	3.36050786167674783997799826083550e-03
21	1.33169515540203788156642166906591e-01	2.72724894316322072325277221844458e-03
22	1.16720933274701291000887725539493e-01	2.20986855953690886419588367706623e-03
23	1.02257431405919038178275031736290e-01	1.78826390264321999398279771128206e-03
24	8.95508127283858594116407019601820e-02	1.44542657328550726857080252749622e-03
25	7.83961028319930614767173088020279e-02	1.16711442195804019558665126539427e-03
26	6.86101566854466616210976539289158e-02	9.41495432894175937842874927421205e-04
27	6.00299941184905270702652324982135e-02	7.58799737152752549854592147665995e-04
28	5.25110331386998700818247974509258e-02	6.10998699362372783997691390696487e-04
29	4.59253281231247667007365599867943e-02	4.91519483298208817983041233383980e-04
30	4.01598777968588267195919995947710e-02	3.94997269772740759120747730149340e-04
31	3.51150396988382900972228874525109e-02	3.17063815302569437242780768838413e-04
32	3.07030693071633025856068326424687e-02	2.54169263655189066241987434556100e-04
33	2.68467901323811952321185618074578e-02	2.03433380026332773186591672337583e-04
34	2.34783937316708681288640025635146e-02	1.62522237707382077096302354822532e-04
35	2.05383642178678839820064784655908e-02	1.29546576264629788075276452826328e-04
36	1.79745193852614117777103084010265e-02	1.02978399018687148172885868196623e-04

(*Continued*)

Table C3
Continued

k	χ_k	γ_k
37	1.57411593704806090331919997928406e-02	8.15827862763857084235776103594481e-05
38	1.37983133839445750806859736203507e-02	6.43623147351034758281773572995289e-05
39	1.21110752013028358188007191935072e-02	5.05118646282732166085507134151195e-05
40	1.06490185910779922966530559824050e-02	3.93819507325944359184298112513636e-05
41	9.38568452652012956402075369290278e-03	3.04490256349179913250724576956079e-05
42	8.29813278439420925351354881096343e-03	2.32914730544885187107604807304053e-05
43	7.36655130339489438745177566237321e-03	1.75702379530898436181417357806391e-05
44	6.57391741813790189283510916305043e-03	1.30132325361793585312305562950935e-05
45	5.90570578080460414802523913159400e-03	9.40281755981180973510534726928533e-06
46	5.34963842759485046283496838777743e-03	6.56579130822932954380944114441017e-06
47	4.89547304507788970804144262729396e-03	4.36542870899759471322771653831421e-06
48	4.53482604688247134485690783763108e-03	2.69520431445801848314129686051970e-06
49	4.26102758786433892841273275905455e-03	1.47390871215592819437170943388163e-06
50	4.06900612679011263031777402788905e-03	6.41931271126488105657466176599801e-07
51	3.95520060861743412410650474994064e-03	1.58535598642490907942230532511450e-07

Table C4

Data for Padé Approximation of the Wave with Velocity $c = 1.0922851405$, the Steepness $H/\lambda = 0.14105777885488320816492860225696$, and $y_b = -0.28978481161845687297742961 1644$. Parameters of Simulations and Padé Approximation are $M = 134217728$, $R(y) \simeq 6.14 \times 10^{-27}$, $err_{pade} \simeq 5.43 \times 10^{-27}$, and the Smallest Fourier Harmonic had Value $|\hat{z}_{k_{max}}| \simeq 3.00 \times 10^{-31}$

k	χ_k	γ_k
1	9.93398643583003025153415435504531e-01	1.28741415762741679346145664996829e-02
2	9.65060482058669453480870980252106e-01	2.60267721567181859054226183119919e-02
3	9.16714789789161849202896809849705e-01	3.43697679627825352269776411757291e-02
4	8.53133231672953078297597841861823e-01	3.81940153445550033591099941584920e-02
5	7.79861194757267505357891461462460e-01	3.83579555843352602595202964927154e-02
6	7.02176870736814955937036169062899e-01	3.59774931820106663192752740784546e-02
7	6.24431910013545641111933110534714e-01	3.21282856711997437340001627375168e-02
8	5.49795332847499273525022520666518e-01	2.76691730121067711930378384900232e-02
9	4.80296232546974823630387324524545e-01	2.31906560517515347893552651709825e-02
10	4.17024645857800791824977075950470e-01	1.90429324287558759377242844714520e-02
11	3.60378305224974615221811203424356e-01	1.53959152585563261217878597243142e-02
12	3.10289842646985418345605736936048e-01	1.23006351687210032636876990145911e-02
13	2.66407648286693861932841258994721e-01	9.73852232172353639036354649203610e-03
14	2.28226886286517332438415939592608e-01	7.65583101348162009153247587551195e-03
15	1.95177843545134733789119725180096e-01	5.98535170044127311114464478095979e-03
16	1.66681805023593130823224346797399e-01	4.65887488461708640776107914945203e-03
17	1.42183993584453030868317439497003e-01	3.61357577121517253016005783742974e-03
18	1.21171172484979583446779037786714e-01	2.79470260489814969664959294926652e-03

(*Continued*)

Table C4
Continued

k	χ_k	γ_k
19	1.03179452511723992079582272565214e-01	2.15617836676118577227243251241331e-03
20	8.77961228595568606401648108610398e-02	1.66012679310648786275121618740345e-03
21	7.46580315447597465030574978595406e-02	1.27592107645668605269203574613739e-03
22	6.34481306443940719507463127666211e-02	9.79089087450639485345366472519338e-04
23	5.38911872290903942028496746096495e-02	7.50248095624531518737269429111365e-04
24	4.57492587887819300483008251206986e-02	5.74148509163471182463355721181721e-04
25	3.88172752742240105088258746631741e-02	4.38854383779301056123215099079188e-04
26	3.29189096590597195144947958198357e-02	3.35061475940689863018834966768472e-04
27	2.79028212558501660025568098114343e-02	2.55540871176311150876065830758264e-04
28	2.36392981742008042750164949870111e-02	1.94691329540109355414952726522057e-04
29	2.00172924085211268884110103807234e-02	1.48182722053010736525844218770677e-04
30	1.69418235041002160106748854919734e-02	1.12674155188771601572543993641392e-04
31	1.43317184931477833930656499987995e-02	8.55924207962470484084537963575900e-05
32	1.21176530092033068365142201489852e-02	6.49586463790799447674548874436684e-05
33	1.02404588173178159766150762312400e-02	4.92531498561398293539370127249816e-05
34	8.64966499042977177325090332415729e-03	3.73103914016284265439688122490895e-05
35	7.30224274879133050003140619052446e-03	2.82375225733516039477667066021446e-05
36	6.16152705009717845830463720403643e-03	2.13513661747602139469739101816769e-05
37	5.19629108350495067218636168760723e-03	1.61297466879220448079982238240246e-05
38	4.37995272297094390520221610919454e-03	1.21739653477311336991048098474804e-05
39	3.68989465744363535075551189083628e-03	9.17991094830884893227377698101798e-06
40	3.10688231013106004394611827804953e-03	6.91584935818872179036239759592572e-06

(*Continued*)

Table C4
Continued

k	χ_k	γ_k
41	2.61456578557885722141496603598660e-03	5.20536938490202499152488268561648e-06
42	2.19905395393225001547396749458147e-03	3.91430351823738560080383189178292e-06
43	1.84855041619759608964615915855160e-03	2.94070847979427725012698794615673e-06
44	1.55304251639257745230445095694940e-03	2.20719808861136536998364371692094e-06
45	1.30403580024761683344961061119599e-03	1.65508232204597074734186170013816e-06
46	1.09432738764763509113618247317394e-03	1.23989163441506187230543611758337e-06
47	9.17812647645417749658202151298786e-04	9.27962520159008244607471765496508e-07
48	7.69320359699922614599799922262156e-04	6.93835226000040035242065190155287e-07
49	6.44472229750674596538655661872796e-04	5.18272340903010891482796683060429e-07
50	5.39563192684084520822965547895566e-04	3.86751562364387865498882802928547e-07
51	4.51459652187210048535645581625337e-04	2.88320243535854856966320396641389e-07
52	3.77512500082907183102947952504772e-04	2.14725698524118689197774299181126e-07
53	3.15483620098192985576130479232556e-04	1.59755495420848083506690922212921e-07
54	2.63483041310020855659728424130368e-04	1.18737501808356300532888071897965e-07
55	2.19915670752623096428691515132722e-04	8.81613507227033650558982811933814e-08
56	1.83436026617218827592565025305802e-04	6.53921058513165146118265854353209e-08

(*Continued*)

Table C4
Continued

k	χ_k	γ_k
57	1.52909808789403664334781521734162e-04	4.84538716133603951388247789431925e-08
58	1.27381290492618707318705788922866e-04	3.58664158964311161459118236867907e-08
59	1.06045663430404223545931459157107e-04	2.65219345830887370991540659742850e-08
60	8.82255960623097328938047290772380e-05	1.95921833026360368361816879242692e-08
61	7.33513735582244917463595672161340e-05	1.44585603393432845280965460758372e-08
62	6.09440811020089107359438382849930e-05	1.06595193757093831390156057934750e-08
63	5.06013718010847795103344003355303e-05	7.85105510061063345075831379965022e-09
64	4.19854284842886757235756347132190e-05	5.77704094551584320668305953789402e-09
65	3.48127867887149603598695647961378e-05	4.24698455656734771613508619208412e-09
66	2.88457365344826502539670719441546e-05	3.11936272695846692633031613888051e-09
67	2.38850607015635551072991988129380e-05	2.28914896008025877293425583671707e-09
68	1.97639074377385155071521574022480e-05	1.67848842336096800302384900691726e-09
69	1.63426213283602794258356970211462e-05	1.22973329115351088076908027814457e-09
70	1.35043863909173156500338815494453e-05	9.00246494394826687766241103823572e-10
71	1.11515555862156824939722316951789e-05	6.58529018137743573464498106258884e-10
72	9.20256064170640198246888785687659e-06	4.81336779425064219659348751354589e-10
73	7.58931213612359462965716406185546e-06	3.51536622960117080648972753857693e-10
74	6.25501349165233025416447266351498e-06	2.56513789011984140244514391180857e-10
75	5.15232409179580442223607363260130e-06	1.86990411531843046778670738725091e-10

(*Continued*)

Table C4
Continued

k	χ_k	γ_k
76	4.24181649775016522927709678588896e-06	1.36150027070583877598207373400005e-10
77	3.49068106812952109834665722037669e-06	9.89896125536513948820894793870582e-11
78	2.87163870904281978123381120499882e-06	7.18405497951763524448150948318652e-11
79	2.36202927278644614134938592885535e-06	5.20148665829541462756399079612847e-11
80	1.94304885285494843909466767533574e-06	3.75443719949043320491081089015406e-11
81	1.59911321065017380641753434790850e-06	2.69886771259819847047462342227678e-11
82	1.31732715240169671433477796333342e-06	1.92941913934894250545144244154976e-11
83	1.08704211469651017023210815498690e-06	1.36906826573455708305877340415078e-11
84	8.99487103028405911079240475052776e-07	9.61543204537063425390253166033986e-12
85	7.47460944734835494603150605681252e-07	6.65765514720154023428202200838344e-12
86	6.25076012803183072949714996778214e-07	4.51781968589147435681661138798625e-12
87	5.27545188407840404034972402364704e-07	2.97790805796735353056158063859767e-12
88	4.51005279547543069512840045259275e-07	1.87970510537824614741588711602232e-12
89	3.92371966727686847652422460137122e-07	1.10896242549626643385666064787054e-12
90	3.49224206935226307895172607412510e-07	5.83901681870167816802893811429244e-13
91	3.19719913320901893897552159916508e-07	2.47055052842115889755229649961340e-13
92	3.02547325679113057732806265306883e-07	5.99062680825025191284334866467265e-14

$R(y) \simeq 10^{-28}$ was found to be sufficient to achieve the desired accuracy of solution in 10^{-26}. After that, we used AGH algorithm with N large enough to make sure that err_{pade} is below 10^{-26} by several orders of magnitude.

The second and third rows in electronic `.dat`-files of Refs. [78, 79] provide the additional information extracted from simulations that include the number of points of the numerical grid $M = 2k_{max}$, the residual $R(y)$, the Stokes wave height y_b at $x = \pm\pi$, the amplitude of the highest Fourier harmonics $|\hat{z}_{k_{max}}|$, the Padé error err_{pade}, the scaled Stokes wave height H/λ, and the Stokes wave velocity c. Values of H/λ are also encoded in the names of `.dat`-files. Also the file `summary.txt` provides a summary of the results from all `.dat`-files.

References

1. G. G. Stokes, On the theory of oscillatory waves, *Trans. Camb. Philos. Soc.* 8: 441–455 (1847).
2. G. G. Stokes, On the theory of oscillatory waves, *Math. Phys. Pap.* 1:197–229 (1880).
3. J. H. Michell, The highest waves in water, *Phil. Mag. Series 5* 36:430–437 (1893).
4. A. I. Nekrasov, On steady waves, *Izv. Ivanovo-Voznesensk. Polytech. Inst.* 3:52–56 (1921).
5. A. I. Nekrasov, *The Exact Theory of Standing Waves on the Surface of Heavy Fluid*, Izdat. Akad. Nauk. SSSR, Moscow, 1951.
6. L. N. Sretenskii, *Theory of Wave Motion of Fluid*, Nauka, Moscow, 1976.
7. M. A. Grant, The singularity at the crest of a finite amplitude progressive Stokes wave, *J. Fluid Mech.* 59(2):257–262 (1973).
8. L. W. Schwartz, Computer extension and analytic continuation of Stokes' expansion for gravity waves, *J. Fluid Mech.* 62(3):553–578 (1974).
9. M. S. Longuet-Higgins and M. J. H. Fox, Theory of the almost-highest wave: The inner solution, *J. Fluid Mech.* 80(4):721–741 (1977).
10. M. S. Longuet-Higgins and M. J. H. Fox, Theory of the almost-highest wave. Part 2. Matching and analytic extension, *J. Fluid Mech.* 85(4):769–786 (1978).
11. J. M. Williams, Limiting gravity waves in water of finite depth, *Phil. Trans. R. Soc. Lond. A* 302(1466):139–188 (1981).
12. J. M. Williams, *Tables of Progressive Gravity Waves*, Pitman, London, 1985.
13. S. Tanveer, Singularities in water waves and Rayleigh–Taylor instability, *Proc. R. Soc. Lond. A* 435:137–158 (1991).
14. S. J. Cowley, G. R. Baker, and S. Tanveer, On the formation of Moore curvature singularities in vortex sheets, *J. Fluid Mech.* 378:233–267 (1999).
15. M. S. Longuet-Higgins, On an approximation to the limiting Stokes wave in deep water, *Wave Motion* 45:770–775 (2008).
16. G. R. Baker and C. Xie, Singularities in the complex physical plane for deep water waves, *J. Fluid Mech.* 685:83–116 (2011).
17. V. E. Zakharov, A. O. Korotkevich, A. Pushkarev, and D. Resio, Coexistence of weak and strong wave turbulence in a swell propagation, *Phys. Rev. Lett.* 99:164501 (2007).

18. V. E. Zakharov, A. O. Korotkevich, and A. O. Prokofiev, On dissipation function of ocean waves due to whitecapping, *AIP Proceedings, CP1168* 2:1229–1231 (2009).
19. V. E. Zakharov, A. I. Dyachenko, and A. O. Prokofiev, Freak waves as nonlinear stage of Stokes wave modulation instability, *Eur. J. Mech. B/Fluids* 25:677–692 (2006).
20. R. C. T. Rainey and M. S. Longuet-Higgins, A close one-term approximation to the highest Stokes wave on deep water, *Ocean Eng.* 33:2012–2024 (2006).
21. W. Drennan, W. Hui, and G. Tenti, Accurate calculations of Stokes water waves of large amplitude, *Zeitschrift fur angewandte Mathematik und Physik* 43:367–384 (1992).
22. G. G. Stokes, Supplement to a paper on the theory of oscillatory waves, *Math. Phys. Pap.* 1:314–326 (1880).
23. J. F. Toland, On the existence of a wave of greatest height and Stokes's conjecture, *Proc. R. Soc. Lond. A* 363:469–485 (1978).
24. P. Plotnikov, A proof of the Stokes conjecture in the theory of surface waves, *Dinamika Splosh. Sredy (In Russian. English translation Stud. Appl. Math. 108:217-244 (2002))* 57:41–76 (1982).
25. C. J. Amick, L. E. Fraenkel, and J. F. Toland, On the Stokes conjecture for the wave of extreme form, *Acta Math.* 148:193–214 (1982).
26. S. Tanveer, Singularities in the classical Rayleigh–Taylor flow: Formation and subsequent motion, *Proc. R. Soc. Lond. A* 441:501–525 (1993).
27. E. Kuznetsov, M. Spector, and V. Zakharov, Surface singularities of ideal fluid, *Phys. Lett. A* 182:387–393 (1993).
28. E. A. Kuznetsov, M. D. Spector, and V. E. Zakharov, Formation of singularities on the free surface of an ideal fluid, *Phys. Rev. E* 49:1283–1290 (1994).
29. A. I. Dyachenko, V. E. Zakharov, and E. A. Kuznetsov, Nonlinear dynamics of the free surface of an ideal fluid, *Plasma Phys. Rep.* 22:829–840 (1996).
30. M. Mineev-Weinstein, P. B. Wiegmann, and A. Zabrodin, Integrable structure of interface dynamics, *Phys. Rev. Lett.* 84:5106–5109 (2000).
31. P. M. Lushnikov, Exactly integrable dynamics of interface between ideal fluid and light viscous fluid, *Phys. Lett. A* 329:49–54 (2004).
32. S. K. Turitsyn, L. Lai, and W. W. Zhang, Asymmetric disconnection of an underwater air bubble: Persistent neck vibrations evolve into a smooth contact, *Phys. Rev. Lett.* 103:124501 (2009).
33. D. W. Moore, The spontaneous appearance of a singularity in the shape of an evolving vortex sheet, *Proc. Roy. Soc. London A: Math. Phys. Eng. Sci.* 365:105–119 (1979).
34. N. A. Inogamov and A. M. Oparin, Bubble motion in inclined pipes, *J. Exp. Theor. Phys.* 97:1168–1185 (2003).
35. S. Wu, Almost global wellposedness of the 2-D full water wave problem, *Invent. Math.* 177:45–135 (2009).
36. S. Wu, Global wellposedness of the 3-D full water wave problem, *Invent. Math.* 184:125–220 (2011).
37. S. A. Dyachenko, P. M. Lushnikov, and A. O. Korotkevich, The complex singularity of a Stokes wave, *JETP Lett.* 98:767–771 (2013).
38. B. Alpert, L. Greengard, and T. Hagstrom, Rapid evaluation of nonreflecting boundary kernels for time-domain wave propagation, *SIAM J. Num. Anal.* 37:1138–1164 (2000).

39. S. R. Lau, Rapid evaluation of radiation boundary kernels for time-domain wave propagation on blackholes: Implementation and numerical tests, *Class. Quant. Grav.* 21:4147–4192 (2004).
40. L. V. Ovsyannikov, Dynamics of a fluid, *M.A. Lavrent'ev Institute of Hydrodynamics Sib. Branch USSR Ac. Sci.* 15:104–125 (1973).
41. D. Meison, S. Orzag, and M. Izraely, Applications of numerical conformal mapping, *J. Comput. Phys.* 40:345–360 (1981).
42. A. I. Dyachenko, E. A. Kuznetsov, M. Spector, and V. E. Zakharov, Analytical description of the free surface dynamics of an ideal fluid (canonical formalism and conformal mapping), *Phys. Lett. A* 221:73–79 (1996).
43. V. E. Zakharov, A. I. Dyachenko, and O. A. Vasiliev, New method for numerical simulation of nonstationary potential flow of incompressible fluid with a free surface, *Eur. J. Mech. B/Fluids* 21:283–291 (2002).
44. B. Chen and P. Saffman, Numerical evidence for the existence of new types of gravity-waves of permanent form on deep-water, *Stud. Appl. Math*. 62:1–21 (1980).
45. P. M. Lushnikov, Branch cuts of Stokes wave on deep water. Part II: Structure and location of branch points in infinite set of sheets of Riemann surface, *ArXiv:1509.03393* (2015).
46. V. I. Petviashvili, Equation for an extraordinary soliton, *Sov. J. Plasma Phys.* 2:257–258 (1976).
47. P. M. Lushnikov, Dispersion-managed soliton in a strong dispersion map limit, *Opt. Lett.* 26:1535–1537 (2001).
48. T. I. Lakoba and J. Yang, A generalized Petviashvili iteration method for scalar and vector Hamiltonian equations with arbitrary form of nonlinearity, *J. Comput. Phys.* 226:1668–1692 (2007).
49. D. Pelinovsky and Y. Stepanyants, Convergence of Petviashvili's iteration method for numerical approximation of stationary solutions of nonlinear wave equations, *SIAM J. Numer. Anal.* 42:1110–1127 (2004).
50. T. Lakoba and J. Yang, A mode elimination technique to improve convergence of iteration methods for finding solitary waves, *J. Comp. Phys*. 226:1693–1709 (2007).
51. J. Yang, Newton-conjugate-gradient methods for solitary wave computations, *J. Comput. Phys.* 228(18):7007–7024 (2009).
52. J. Yang, *Nonlinear Waves in Integrable and Nonintegrable Systems*, SIAM, Philadelphia, PA, USA, 2010.
53. T. Lakoba, Conjugate gradient method for finding fundamental solitary waves, *Physica D* 238:2308–2330 (2009).
54. M. R. Hestenes and E. Stiefel, Methods of conjugate gradients for solving linear systems, *J. Res. Nat. Bur. Stand.* 49:409–436 (1952).
55. D. G. Luenberger, The conjugate residual method for constrained minimization problems, *SIAM J. Numer. Anal.* 7:390–398 (1970).
56. J. Yang and T. Lakoba, Accelerated imaginary-time evolution methods for the computation of solitary waves, *Stud. Appl. Math.* 120:265–292 (2008).
57. I. S. Gandzha and V. P. Lukomsky, On water waves with a corner at the crest, *Proc. Roy. Soc. A* 463:1597–1614. (2007).
58. B. Alpert, L. Greengard, and T. Hagstrom, Rapid evaluation of nonreflecting boundary kernels for time-domain wave propagation, *SIAM J. Sci. Comp.* 20:1551–1584 (1999).
59. A. Markoff, Deux démonstrations de la convergence de certaines fractions continues, *Acta Math.* 19:93–104 (1895).

60. R. de Montessus de Ballore, Sur les fractions continues algébriques, *Bull. Soc. Math. France* 30:28–36 (1902).
61. V. I. Buslaev, Simple counterexample to the Baker–Gammel–Wills conjecture, *East J. Approx.* 7:515–517 (2001).
62. D. S. Lubinsky, Rogers–Ramanujan and the Baker–Gammel–Wills Padé conjecture, *Ann. Math.* 157:847–889 (2003).
63. J. Nuttall, The convergence of Padé approximants of meromorphic functions, *J. Math. Anal. Appl.* 31:147–153 (1970).
64. A. A. Gonchar, On the convergence of Padé approximants, *Math. USSR Sb.* 21:155–166 (1973).
65. A. A. Gonchar, On the convergence of generalized Padé approximants of meromorphic functions, *Math. USSR Sb.* 27:503–514 (1975).
66. H. Stahl, Extremal domains associated with an analytic function, I, *Comp. Var. Theory Appl.* 4:311–324 (1985).
67. H. Stahl, Extremal domains associated with an analytic function, II, *Comp. Var. Theory Appl.* 4:321–338 (1985).
68. H. Stahl, The convergence of Padé approximants to functions with branch points, *J. Approx. Theory* 91:139–204 (1997).
69. A. I. Aptekarev, V. I. Buslaev, A. Martinez-Finkelshtein, and S. Suetin, Padé approximants, continued fractions, and orthogonal polynomials, *Russian Math. Surv.* 88:1049–1131 (2011).
70. E. B. Saff, An extension of Montessus de Ballore's theorem on the convergence of interpolating rational functions, *J. Approx. Theory* 6:63–67 (1972).
71. J. G. A. Baker and P. R. Graves-Morris, *Padé Approximants*, 2nd ed., Cambridge University Press, Cambridge, 1996.
72. P. Gonnet, R. Pachon, and L. N. Trefethen, Robust rational interpolation and least-squares, *Electron. Trans. Numer. Anal.* 1388:146–167 (2011).
73. F. D. Gakhov, *Boundary Value Problems*, Pergamon Press, New York, 1966.
74. A. D. Polyanin and A. V. Manzhirov, *Handbook of Integral Equations: Second Edition*, Chapman and Hall/CRC, Boca Raton, 2008.
75. M. Frigo and S. G. Johnson, The design and implementation of FFTW 3, *Proc. IEEE* 93:216–231, URL http://fftw.org (2005).
76. *GNU Project*, URL http://gnu.org (1984–2016).
77. V. E. Zakharov, Stability of periodic waves of finite amplitude on a surface, *J. Appl. Mech. Tech. Phys.* 9:190–194 (1968).
78. S. A. Dyachenko, P. M. Lushnikov, and A. O. Korotkevich, Library of Stokes waves, URL http://stokeswave.org (2015).
79. S. A. Dyachenko, P. M. Lushnikov, and A. O. Korotkevich, "Branch cuts of Stokes wave on deep water. Part I: Numerical solution and Pade approximation", arXiv:1507.02784, URL http://arxiv.org/abs/1507.02784, (2015).

University of Illinois at Urbana-Champaign
University of Arizona
University of New Mexico
Landau Institute for Theoretical Physics

(Received September 2, 2015)